

Modelling Transport of Non-Spherical Particles in Laminar Flow

Elise Holmstedt

Modelling transport of non-spherical particles in laminar flow

Elise Holmstedt

Division of Fluid and Experimental Mechanics
Department of Engineering Sciences and Mathematics
Luleå University of Technology
SE-971 87 Luleå, Sweden

Printed by Luleå University of Technology, Graphic Production 2014

ISSN 1402-1757

ISBN 978-91-7583-182-4 (print)

ISBN 978-91-7583-183-1 (pdf)

Luleå 2014

www.ltu.se

ABSTRACT

A model has been developed that can be used to predict the transport of non-spherical particles in the nano- and micro scale range for different applications. This may be the flow in the lungs or flow taking place during composites manufacturing, but the model can be applied to many applications where the particle Stokes and Reynolds numbers are small. The model can, for instance, be used to simulate an evenly random distribution of particles and then follow them through a laminar flow in a straight circular tube, either to study the statistical congregation of multiple particles or to follow the path of an individual particle. Both gravitational settling and Brownian motions are included in the model and their influence was also examined.

To increase the understanding of the influence of the breathing pattern on the deposition of inhaled nano- and micro-fibres simulations were done in a straight model airway. Maximum deposition rate was found when particles were released in the beginning of the respiratory cycle while a minimum when the release came at the peak of inhalation. A comparison was done of a cyclic flow field and a quasi-steady one to see if the latter could accurately be used to replace the former. A quasi-steady solution generally provides a relatively good approximation to cyclic flow if an average velocity over one residence time of the particles moving with the mean fluid velocity is used.

A statistical study was done to compare the deposition rates of oblate and prolate particles of different size and aspect ratio as they travel down narrowing bronchi in a steady, fully developed parabolic flow field. The model shows a clear correlation between increased particle size and increased deposition, it also consistently yielded a higher deposition rate for oblate particles compared to prolate particles with a similar geometric diameter. A study of the motion and orientation of single oblate and prolate particles with large aspect ratio and the same geometric diameter has also been done. To see the effect the different forces have on the particle it was first studied with only the force of the flow field acting on it. Clear Jeffery orbits were visible in the simulations, although the periods of the orbits were shorter for the oblate particles than the prolate ones. When Brownian motion was introduced the motion of the particles became less periodic. For prolate particles Jeffery orbits could still be distinguished, unlike for the oblate particles whose movements mostly resembled random tumbling.

In some methods to produce fibre reinforced polymer composites a fabric is impregnated with a fluid that may contain particles on the micro- and nano scales. These particles are aimed to give the final product additional properties. It is therefore interesting to be able to reveal how the distribution and orientation of such particles are affected by the processing condition. During the manufacturing of the fabric and during

the subsequent lay-up in a mold relatively large channels are formed between bundles of fibres where the impregnating fluid flows; there is also micro channels within the bundle that are also impregnated by the fluid and the capillary action there may be modelled as a suctioning force on the walls of the channels. Therefore in this study the channel between the bundles are represented as a tube with a circular diameter and a flow field that are being sucked to the sides as it travels down the tube. A random distribution of particles is introduced at the inlet of the channel and the deposition is studied and the results are compared to a case when the flow is purely driven by an applied pressure gradient without any suction on the walls.

PREFACE

This work was carried out at the Division of Fluid and Experimental mechanics at Luleå University of Technology during the years 20012-20014 and funded by the Swedish Research Council.

I am very grateful to have had Staffan Lundström and Hans Åkerstedt as my supervisors, you made this work possible. I also want to thank my predecessor Sofie Högberg whose code is the foundation to my work and whose thesis is the most read book at my desk.

I want to thank my colleagues and friends here at Fluid and Experimental mechanics for welcoming me and giving me a place to belong - and for making sure I eat at least one cocked meal a day. Also those of you at Machine elements, my first home here at LTU, for keeping me around even after I moved out.

My family and friends, the best support anyone could ever wish for. My parents, for being the one thing I can always count on. And Andrew; you push me in just the right way.

Luleå, November 2014
Elise Holmstedt

APPENDED PAPERS

Paper A

Time-Dependent Deposition of Micro- and Nanofibers in Straight Model Airways. Sofie M. Högberg, Hans O. Åkerstedt, Elise Holmstedt, T. Staffan Lundström, Thomas Sandström *Journal of Fluids Engineering, Trans. ASME J. Fluids Eng, 2012, 134(5)*

Paper B

Modelling transport and deposition rate of oblate and prolate nano- and micro particles in a virtual model of the human airway. 2014. Elise Holmstedt, Hans O. Åkerstedt, T. Staffan Lundström *Submitted to Journal of Fluids Engineering*

Paper C

Modelling transport and deposition of non-spherical micro- and nano-particles in composite manufacturing. 2014. Elise Holmstedt, Hans O. Åkerstedt, T. Staffan Lundström *Manuscript*

Time-Dependent Deposition of
Micro- and Nanofibers in Straight
Model Airways

Authors:

Sofie M. Högberg, Hans O. Åkerstedt, Elise Holmstedt, T. Staffan Lundström, Thomas Sandström

Journal of Fluids Engineering, Trans. ASME J. Fluids Eng, 2012, 134(5)

Sofie M. Högborg
Hans O. Åkerstedt
Elise Holmstedt
T. Staffan Lundström¹
e-mail: staffan.lundstrom@ltu.se

Fluid Mechanics,
Luleå University of Technology,
SE-97187, Luleå, Sweden

Thomas Sandström
Department of Public Health
and Clinical Medicine,
Division of Medicine,
Umeå University,
SE-90185, Umeå, Sweden

Time-Dependent Deposition of Micro- and Nanofibers in Straight Model Airways

In this paper, we increase the understanding of the influence of the breathing pattern on the fate of inhaled non-spherical micro and nanoparticles and examine the accuracy of replacing the cyclic flow field with a quasi-steady flow. This is done with new analysis and numerical simulations on straight model airways using a previously developed discrete model for fiber motion. For the conditions studied, maximum deposition is obtained when fibers are released at the start of the inspiratory cycle, and minimum is received at the peak of inhalation. A quasi-steady solution generally provides a relatively good approximation to cyclic flow if an average velocity over one residence time of the particles moving with the mean fluid velocity is used. For a batch type, supply of particles deposition is favored in light activity breathing as compared to heavy breathing and the inclusion of a short pause after the inhalation results in an increased deposition in the terminal bronchiole. During zero-flow over the time of a breathing pause, spherical 10 nm particles experience considerable deposition in the distal airways, whereas only a few percent of larger and/or fibrous nanoparticles were deposited. Hence, size and shape are crucial variables for deposition for no flow conditions. Common for all breathing parameters examined was that minimum deposition was obtained for the spherical 1 μ m-particles and the fibrous 100 nm-particles. The former is expected from studies on spherical particles, and the latter is in agreement with results from a recent publication on steady inspiration. [DOI: 10.1115/1.4006698]

Introduction

Knowledge of how various factors determine the fate of inhaled particles is of great importance both in health risk assessments on undesirable aerosols such as air pollution [1,2] and for manufacturers of inhalers with therapeutic aerosols. The extent and location of particle deposition depend on particle size, density, and shape, airway geometry, and the individual's breathing pattern [3]. Regarding the latter, the complexity of simulating the actual breathing cycle is often avoided by replacing it with a constant inspiratory flow, especially for cases where complex or relatively large systems of airways are studied (see Zhang et al. [4] and Walters and Luke [5], respectively). There are a number of studies published on oscillatory flow of larger spherical particles, for which Brownian motion can be neglected [6]. Zhang et al. [7] examined how inertial impaction affected the deposition of spherical micro in a triple bifurcation airway model at laminar oscillatory inhalation flow using a commercial finite-volume code and found that particle deposition efficiency was typically larger for cyclic flow than for steady flow at the mean flow rate of a given inhalation pulse. Kim and Fisher [8] performed experiments on the same area with the main conclusion that deposition efficiency increased with the Stokes number and that the bifurcation geometry matters. In Zhang et al. [9], the study presented in Zhang et al. [7] was extended to include spherical nanoparticles and the simulations were validated with experiments. Differences in deposition between transient and steady cases were highlighted but it was concluded that with a proper choice of flow rates, the total deposition can be very similar between transient and steady cases. Experimental results by Myojo [10] yielded that deposition fraction of microparticles increased with 1.4–1.7 times for cyclic flow as

compared to steady flow. Kojic and Tsuda [11] investigated the effects of gravitational settling in oscillatory pipe flow and concluded that oscillating flow must be considered when the time for gravitational sedimentation is in the same range as the time for flow oscillation. They also state that the vertical sedimentation of spherical micro particles in a straight pipe is entirely independent of the axial flow, neglecting Saffmans lift force [12]. This is not the case for non-spherical particles since their orientation is influenced by the flow, and the drag in its turn is dependent on the orientation. To the authors' best knowledge, there are no publications available on simulations of cyclic inhalation and deposition of non-spherical micro- or nanoparticles.

In previous publications [13,14], we presented a semi-analytical model for respiratory transport and deposition of fibrous micro- and nanoparticles, and successfully validated this model with well-known simpler models for diffusion and sedimentation [15,16] and models based on a continuous approach [17]. In the present work, we apply the fiber model on straight model airways with transient velocity field without secondary flow [18–20] representing an inhalation and following pause. The problem is solved numerically with MATLAB, and the velocity field is defined with an analytical solution. The aims of this work are to increase the understanding of the influence of the breathing pattern on the fate of inhaled particles of various shapes, and to examine the accuracy of replacing the cyclic flow field with a constant inspiratory flow.

The Importance of Unsteadiness

Depending on the characteristics of the flow, a steady velocity field may be a good approximation for the motion of fluids as well as particles carried by the fluid. The relative importance of unsteadiness in laminar oscillatory flow can be determined from the Womersley number $\alpha = R\sqrt{n/\nu}$, which arises in the solution of the exact Navier Stokes equations for oscillatory flow when comparing the unsteady term to the viscous term. Here, R is a

¹Corresponding author.

Contributed by the Fluids Engineering Division of ASME for publication in the JOURNAL OF FLUIDS ENGINEERING. Manuscript received September 7, 2011; final manuscript received March 18, 2012; published online May 22, 2012. Assoc. Editor: Kendra Sharp.

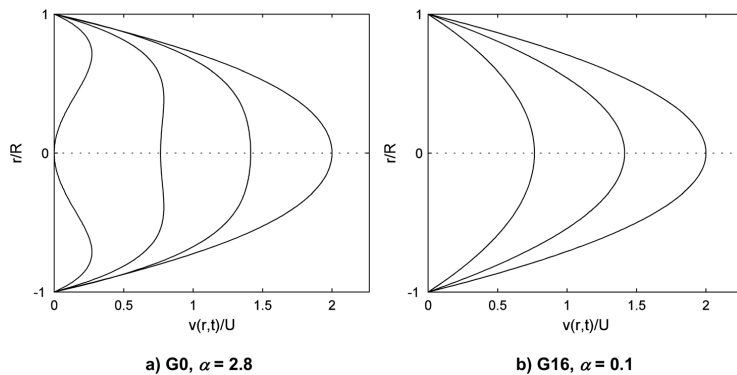


Fig. 1 Velocity profiles at $nt = 0, \pi/8, \pi/4, \pi/2$ for Weibel's generation 0 (G0, $\alpha = 2.8$) and 16 (G16, $\alpha = 0.1$) at light activity breathing

characteristic length (the airway radius in this context), $n (=2\pi f)$ is the angular frequency, and ν is the kinematic viscosity of the fluid. For small Womersley number flows ($\alpha^2 \leq 1$) the frequency of the oscillations is low enough for a parabolic velocity profile to develop during each cycle, and thus Poiseuille flow using the instantaneous pressure gradient is a good approximation. For large Womersley number flows on the other hand, the velocity profile is relatively flat and closer to a developing profile.

As we proceed from the proximal airways down the tracheo-bronchial tree, the airway radii are getting progressively smaller. Thus, for the alveolar region and much of the distal tracheobronchial region, the unsteady terms in the Navier-Stokes equations are expected to be small, implying small α , at normal breathing. This assertion is, however, based on using the average value of the unsteady term. At times when the velocity is small while its rate of change is relatively large, as is the case at the start-up of an inhalation and at times between inhalation and exhalation, the unsteady terms in the fluid equations may not be neglected. In such cases, the unsteadiness in the fluid dynamics may need to be included to adequately model aerosol deposition. Furthermore, even when unsteady effects are unimportant in the fluid equations, such effects may still be important in determining particle deposition.

The time a particle is present in an airway of a certain generation, the so called particle residence time, can be approximated as $t_{res} = L/U$, where L is the length of the airway and U is the average fluid velocity in the airway over the time the particle is in that generation. If the fluid velocity does not change a lot during this time, such that $\Delta U/U$ is small, the particle sees little variation in the velocity field and the deposition can be expected to be close to that predicted from using a steady velocity equal to the value of the velocity at that time in the breathing cycle. If $\Delta U/U$ is not small, however, an unsteady velocity field may be required to predict the particle deposition in that generation [21]. This may certainly be the case for the application of the present work.

Theoretical Background

In this section, we briefly provide the governing equations for the velocity field in transient pipe flow, the equations for the fiber motion and the conditions for the simulations.

Velocity Profile for Transient Pipe Flow. The velocity field is obtained from an analytic solution for unsteady flow in a circular pipe [22]. Let y be the coordinate along the axis of the pipe and r the distance from the center, then if the pipe is assumed long enough for the solution to be independent of y , the Navies-Stokes equations in cylindrical coordinates reduce to

$$\frac{\partial v}{\partial t} = -\frac{1}{\rho} \frac{\partial p}{\partial y} + \nu \left(\frac{\partial^2 v}{\partial r^2} + \frac{1}{r} \frac{\partial v}{\partial r} \right) \quad (1)$$

with no-slip boundary condition on the airway walls. Here, v is the axial velocity component, p is the fluid pressure, and ρ is the fluid density. For an oscillating pressure gradient

$$-\frac{1}{\rho} \frac{\partial p}{\partial y} = K \sin nt \quad (2)$$

we obtain the solution

$$v(r, t) = -\frac{K}{n} e^{int} \left[1 - \frac{J_0(r\sqrt{-in/\nu})}{J_0(R\sqrt{-in/\nu})} \right] \quad (3)$$

where J_0 is the zeroth order Bessel function and K is a constant. To solve for the fiber motion we will also need the space derivatives

$$\frac{\partial v}{\partial x} = \frac{x}{r} \frac{\partial v}{\partial r}; \quad \frac{\partial v}{\partial z} = \frac{z}{r} \frac{\partial v}{\partial r} \quad (4)$$

with

$$\frac{\partial v}{\partial r} = -\frac{K}{n} \sqrt{-in/\nu} \frac{J_1(r\sqrt{-in/\nu})}{J_0(R\sqrt{-in/\nu})} \quad (5)$$

The velocity and corresponding space derivatives are given in complex form above, but only the real part will be used since the imaginary part lacks physical relevance. The shape of the velocity profile over the airway cross-section is shown for various phases of the inhalation for trachea, referred to as Weibel's generation 0 (G0), and terminal bronchiole (G16) in Fig. 1. Here, the influence of the Womersley number is evident.

Fiber Equations of Motion. The model for the fiber motion is described in detail in Ref. [13], and only a brief summary considered relevant to the understanding of the underlying model is given here. Also, as the focus is on nanofibers in the present work, details of the important forces on microfibers, for instance, are excluded but can be found in the original work [13]. Two coordinate frames are defined; a global coordinate system $[x, y, z]$ fixed in space and a local coordinate system $[x', y', z']$ fixed to the fiber, with the fiber polar axis along z' . Now let a rotation matrix \mathbf{A}

transform from local to global coordinates so that if a vector \mathbf{x}' is considered, the matrix \mathbf{A} may be used to obtain its components in the rotated global coordinate system via $\mathbf{x}' = \mathbf{A}\mathbf{x}$. The equations of motion for the fibers are given by the equations for the translational motion

$$\begin{bmatrix} \frac{dx}{dt} \\ \frac{dy}{dt} \\ \frac{dz}{dt} \end{bmatrix} = \begin{bmatrix} u \\ v \\ w \end{bmatrix} + \mathbf{A}^T \begin{bmatrix} v_{Br,x'}(t) \\ v_{Br,y'}(t) \\ v_{Br,z'}(t) \end{bmatrix} \quad (6)$$

and the equations for the rotational motion may be written as

$$\omega_{x'} = \xi' - \frac{\beta^2 - 1}{\beta^2 + 1} \dot{\epsilon}_{y'z'} + \chi'_{x'} \sqrt{\frac{2D_{\perp}'}{\delta t}} \quad (7)$$

and

$$\omega_{y'} = \eta' + \frac{\beta^2 - 1}{\beta^2 + 1} \dot{\epsilon}_{x'z'} + \chi'_{y'} \sqrt{\frac{2D_{\perp}'}{\delta t}} \quad (8)$$

Rotation about the fiber major axis z' does not affect fiber transport due to the fiber rotational symmetry and hence is excluded in the analysis. In Eq. (6), $[dx/dt, dy/dt, dz/dt]$ are the components of the fiber velocity, $[u, v, w]$ are the components of the fluid velocity, and

$$v_{Br,i'}(t) = \chi_{i'}' \sqrt{\frac{2D_{i'}'}{\delta t}} \quad (9)$$

is the Brownian diffusion velocity. Furthermore, δt is a Brownian time increment, $\chi_{i'}'$ is a standard normally distributed random number, and

$$D_{i'}' = \sigma T / 3\pi\mu d_f \quad (10)$$

is the translational diffusion coefficient. Here, d_f denotes the Stokes diameters and these are given by

$$d_{\parallel} = \frac{\frac{4}{3}(\beta^2 - 1)d_f}{C_{\parallel}' \left[\frac{2\beta^2 - 1}{\sqrt{\beta^2 - 1}} \ln \left(\beta + \sqrt{\beta^2 - 1} \right) - \beta \right]} \quad (11)$$

$$d_{\perp} = \frac{\frac{8}{3}(\beta^2 - 1)d_f}{C_{\perp}' \left[\frac{2\beta^2 - 3}{\sqrt{\beta^2 - 1}} \ln \left(\beta + \sqrt{\beta^2 - 1} \right) + \beta \right]} \quad (12)$$

for a fiber oriented parallel and perpendicular to the direction of motion, respectively. σ is the Boltzmann constant, T is the absolute temperature of the fluid, β is the fiber aspect ratio (length to diameter), d_f is the geometric fiber diameter, and $C_{i'}'$ is the slip correction factor.

In Eqs. (7)–(8), $[\omega_{x'}, \omega_{y'}]$ are the components of the fiber angular velocity, and the last term on the right hand side of these equations denotes the Brownian angular velocity, with

$$D_{\perp}' = \sigma T B_{\perp}' \quad (13)$$

being the rotational diffusion coefficient. The angular mobility is given by

$$B_{\perp}' = \frac{3C_{\perp}' \left[\frac{2\beta^2 - 1}{\sqrt{\beta^2 - 1}} \ln \left(\beta + \sqrt{\beta^2 - 1} \right) - \beta \right]}{2\pi\mu d_f^3 (\beta^4 - 1)} \quad (14)$$

where μ is the dynamic viscosity and C_{\perp}' is the rotational slip correction factor. Expressions for both the translational and rotational diffusion coefficients are found in Ref. [13], and for the nanofibers they are close to unity. Furthermore, $\dot{\epsilon}_{ij} = \frac{1}{2} \left(\frac{\partial u_i}{\partial x_j} + \frac{\partial u_j}{\partial x_i} \right)$ are the elements of the deformation rate and $[\xi, \eta, \zeta]^T = \frac{1}{2} (\nabla \times \mathbf{u})$ are the spin tensors. The latter two are received in global coordinates from the solution of the flow field, and the local equivalents are found by the transformations

$$\dot{\epsilon}_{i'j'} = \mathbf{A} \dot{\epsilon}_{ij} \mathbf{A}^T; \quad [\xi', \eta', \zeta']^T = \mathbf{A} [\xi, \eta, \zeta]^T \quad (15)$$

Fiber rotation is represented with quaternions [23,24] that consist of four parameters describing the evolution of fiber orientation using a unit vector for the axis of rotation and an angle of rotation around that axis. Following the derivation in Ref. [13], we obtain the rotation matrix

$$\mathbf{A} = 2 \begin{bmatrix} q_1^2 + q_4^2 - \frac{1}{2} & q_1q_2 + q_3q_4 & q_1q_3 - q_2q_4 \\ q_1q_2 - q_3q_4 & q_2^2 + q_4^2 - \frac{1}{2} & q_2q_3 + q_1q_4 \\ q_1q_3 + q_2q_4 & q_2q_3 - q_1q_4 & q_3^2 + q_4^2 - \frac{1}{2} \end{bmatrix} \quad (16)$$

The coefficients of the quaternion, q_1 to q_4 , can be computed from the Euler angles provided for the initial orientation using the relations [23,24]

$$q_1 = \sin \frac{\theta}{2} \cos \frac{\phi - \psi}{2} \quad (17)$$

$$q_2 = \sin \frac{\theta}{2} \sin \frac{\phi - \psi}{2} \quad (18)$$

$$q_3 = \cos \frac{\theta}{2} \sin \frac{\phi + \psi}{2} \quad (19)$$

$$q_4 = \cos \frac{\theta}{2} \cos \frac{\phi + \psi}{2} \quad (20)$$

where (ϕ, θ, ψ) are the Euler angles obtained using the x -convention [23]. The quaternion coefficients can then be updated in every time step with

$$\begin{bmatrix} \dot{q}_1 \\ \dot{q}_2 \\ \dot{q}_3 \\ \dot{q}_4 \end{bmatrix} = \frac{1}{2} \begin{bmatrix} q_4 & -q_3 & q_2 & q_1 \\ q_3 & q_4 & -q_1 & q_2 \\ -q_2 & q_1 & q_4 & q_3 \\ -q_1 & -q_2 & -q_3 & q_4 \end{bmatrix} \begin{bmatrix} \omega_{x'} \\ \omega_{y'} \\ 0 \\ 0 \end{bmatrix} \quad (21)$$

Simulation Conditions. We consider cyclic and quasi-steady laminar flow in straight horizontal airways with dimensions according to Weibel's model A [25], for which results will be presented for both light and heavy activity levels. For the light activity level, a tidal volume, V_T , of 750 ml is used and a respiratory cycle of 4 s duration is assumed. The latter includes an inhalation, an exhalation and a pause in between, in total corresponding to a respiratory frequency of 15 min^{-1} and a tracheal flow rate $Q_{\text{light}} = 25.9 \text{ l/min}$. The inspiratory portion of the cycle, t_{in} , is assumed to be 1.74 s, and on the basis of pneumotachographic data the length of the pause after inhalation is taken to be 5% of the total respiratory cycle, i.e., 0.2 s for this level of activity. This definition of the respiratory cycle corresponds to that described by the Task Group on Lung Dynamics in ICRP [26]. For the heavy

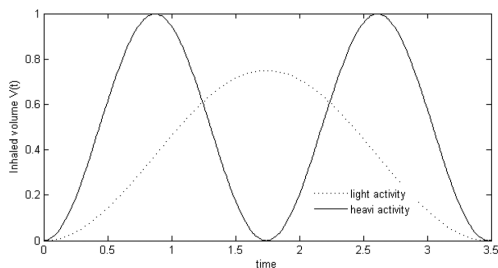


Fig. 2 Inhaled volume versus time for light and heavy activity

activity breathing, a volumetric flow rate of 60 liters/min and a respiratory frequency of 30 min^{-1} are set, whereby $t_{in} = 0.87 \text{ s}$.

The actual respiration profiles for light and heavy breathing conditions are presented in Fig. 2. The volumetric flow rate is expressed as

$$Q(t) = \int_0^R v(r, t) 2\pi r dr \quad (22)$$

and the inhaled volume versus time is given by

$$V(t) = \int_0^t Q(t) dt \quad (23)$$

The constant K in Eq. (3) may now be derived from the condition that the inhaled volume $V(t)$ after time t_{in} is V_{in} according to

$$V(t_{in}) = V_{in}$$

Notice that since the volumetric flow rate in an airway of generation Z is given by $Q_Z = \frac{Q}{2^Z}$, where the tracheal flow rate is Q , K in Eq. (3) can be computed for each generation. In the simulation results that follow, we have considered the inspiratory part of the breathing cycle and a subsequent pause. Additionally, the fiber behavior for zero-flow in the distal airways is scrutinized.

Deposition due to gravitational settling, Brownian motion and interception is considered, and the deposition efficiency, DE , is defined as the quotient of the number of fibers that are deposited in an airway of specified generation (within a given time), and the number of fibers that are injected. Deposition results are based on simulations of 10,000 particles. In a previous paper we found that 100,000 particles were required to obtain results that are independent of fiber initial conditions; the error introduced when using 10,000, however, is considered small enough for our purposes. If not stated otherwise, results are for light activity breathing.

Results and Discussion

Influence of the Moment of Fiber Injection and of Quasi-Steady Versus Cyclic Flow. Maximum deposition is obtained when fibers are released at the start of the inspiratory cycle, and the minimum is received at the peak of inhalation ($nt = \pi/2$), i.e. when the flow rate is highest. Figures 3–5 show the deposition efficiency as a function of injection time for Weibel's generation

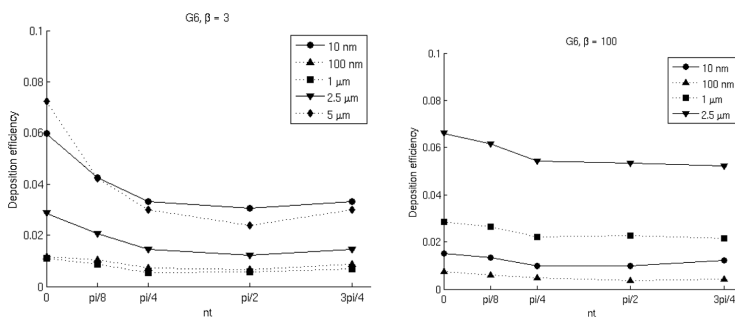


Fig. 3 Deposition efficiency in Weibel's G6 for fibers with $\beta = 3$ (left) and $\beta = 100$ (right) as a function of moment of fiber injection

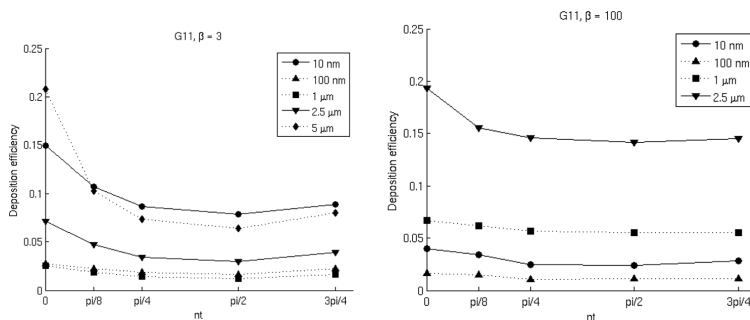


Fig. 4 Deposition efficiency in Weibel's G11 for fibers with $\beta = 3$ (left) and $\beta = 100$ (right) as a function of moment of fiber injection

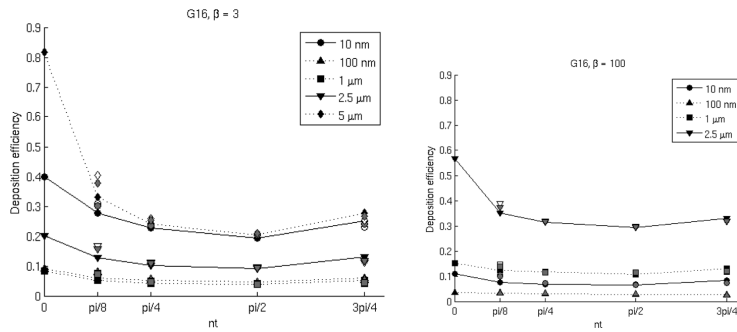


Fig. 5 Deposition efficiency in Weibel's G16 ($\alpha = 0.1$) for fibers with $\beta = 3$ (left) and $\beta = 100$ (right) as a function of moment of fiber injection. Non-filled and gray symbols represent quasi-steady solution with initial and mean velocity approximation, respectively.

Table 1 Average residence times based on average fluid velocity for different generations, activity and time of injection

Generation	Activity	Phase of injection $\pi/8$	Phase of injection $\pi/4$	Phase of injection $\pi/2$
6	Light	0.137	0.074	0.052
11	Light	0.028	0.016	0.011
16	Light	0.112	0.063	0.045
6	High	0.044	0.024	0.017
11	High	0.010	0.006	0.004
16	High	0.039	0.021	0.015

6, 11, and 16. The dimensions of the different airways of the Weibel's generations used are given in the Appendix.

This finding is in agreement with simple analysis since the particle settling distance is proportional to t and the displacement due to Brownian motion is proportional to \sqrt{t} , thus deposition of both micro- and nanoparticles is favored by longer residence time. Steady-state simulations with Poiseuille flow, with the mean velocity set to that for the cyclic flow field at the time of fiber injection, generally overestimated fiber deposition when fibers were injected before the peak velocity was reached, see non-filled symbols in Fig. 5. This is also reasonable since, in this case, the fibers do not experience the small increase in velocity that they do in the cyclic simulation. With the same reasoning, the opposite behavior was observed if fibers were injected after the peak (see Fig. 5 for deposition in Weibel's generation 16 (G16)). The best agreement is achieved for fibers injected at the peak velocity, which is expected since this is where we have the shortest particle residence times, and thus particles only see little changes in the velocity field as long as they are within the airway. A better steady flow approximation of the cyclic flow is to use a steady velocity averaged over one residence time, in which the residence time is calculated from the particles moving with the mean fluid velocity, see the gray symbols in Fig. 5; see also Table 1.

As obvious from Figs. 3–5, the deposition is influenced by parameters such as particle characteristics and airway generation, and the trends are in agreement with those presented for steady inspiratory flow [13]; the deposition efficiency generally increases with airway generation number and the lowest deposition efficiency was obtained for spherical $1 \mu\text{m}$ -particles and fibrous 100 nm-particles, for instance.

Light versus Heavy Activity Level. To examine the influence of the level of activity on the behavior of inhaled particles, simulations were performed both at conditions of light and heavy activity breathing, for which fibers were either injected at the start of an inhalation or at the peak velocity ($t_{in}/2$), and results refer to the deposition that took place over one inhalation. The deposition

of nanoparticles in one inhalation was in all cases higher at light activity breathing as compared to heavy activity breathing, which is reasonable since the time over which the inhaled fibers can deposit is longer for the lower flow rate (see Table 2). Using the results in Table 2, a pairwise comparison with a student t-test yields a 99.9% probability that the light activity deposition is higher than the heavy activity deposition. In addition, for the microparticles, all results indicate that the light activity deposition is higher, and a student t-test in this case yields a probability of 99.2% that this is true (see Table 3). This result holds for a batch type of supply of particles. The relatively large difference in deposition as a function of activity level confirms that it is possible to target and optimize drug delivery as to breathing pattern in addition to aerosol, composition, size and shape, [9,27,28]. Note, however, that the respiratory frequency for heavy activity is twice the one for light activity. Hence, for a continuous supply of particles,

Table 2 Deposition of nanoparticles in one inhalation for light and heavy activity level

Gen	α (heavy, light)	d_f [μm]	β	Inject at $t = 0$		Inject at $t = t_{in}/2$	
				DE _{heavy} (%)	DE _{light} (%)	DE _{heavy} (%)	DE _{light} (%)
6	0.61,0.43	0.01	3	3.8	5.4	1.8	2.8
			100	1.1	1.7	0.4	0.9
			0.1	0.8	1.2	0.39	0.77
11	0.24,0.17	0.01	3	9.5	14.4	4.7	7.1
			100	2.7	3.9	1.4	2.4
			0.1	1.8	2.6	0.93	1.6
16	0.13,0.09	0.01	3	22.8	39.2	11.8	20.5
			100	6.0	10.9	3.6	6.4
			0.1	4.5	8.4	2.7	4.6
			100	2.7	4.0	1.6	2.8

Table 3 Deposition of microparticles in one inhalation for light and heavy activity level

Gen	d_f [μm]	β	Inject at $t = 0$		Inject at $t = t_{in}/2$	
			DE _{heavy} (%)	DE _{light} (%)	DE _{heavy} (%)	DE _{light} (%)
6	1.0	3	0.46	0.85	0.22	0.56
		100	2.3	2.9	1.7	2.4
		3	1.3	2.4	0.61	1.2
11	2.5	100	5.5	7.2	3.7	5.2
		3	3.2	6.3	1.2	2.2
		3	1.2	2.0	0.61	1.2
16	5.0	100	15.2	18.5	12.3	14.1
		3	9.2	16.4	3.2	5.4
		3	3.74	7.98	1.71	4.09
16	1.0	100	10.86	15.57	9.89	11.42
		3	9.06	19.27	4.2	9.23
		100	31.43	56.11	27.3	29.29
16	2.5	3	25.47	80.82	9.2	20.4
		3				
		3				

Table 4 Impact of adding a pause after the inhalation

d_f [μm]	β	Inhalation		Inhalation + pause	
		DE (%)	Susp (%)	DE (%)	Susp (%)
0.01	3	39.2	0.18	39.1	0.11
	100	10.9	1.4	11.1	1.2
0.1	3	8.4	3.6	8.4	3.1
	100	4.0	8.0	3.6	8.1
1.0	3	8.0	3.8	8.4	3.5
	100	15.6	0.20	15.4	0.08
2.5	3	19.3	0.06	20.9	0.02
	100	56.1	1.6	56.4	1.7
5.0	3	80.8	0.45	81.2	0.66

the results suggest that the delivered dose is higher for the higher activity level with probabilities of 95.1% and 91.4% for nano- and microparticles, respectively. One obvious reason to this is that the amount of particles inhaled in two inhalations at heavy activity breathing exceeds that inhaled in one inhalation at light activity. The overall high probability values show that we can be very confident in these results (see Tables 2 and 3).

Influence of Adding a Pause Following the Inhalation. So far, we have only considered the inspiratory part of the respiratory cycle. The ultimate goal would be to simulate a whole breathing cycle, or even multiple breaths. Since that is extremely complex, one option is to include a pause after the inhalation. Under the conditions studied, this only influenced fibers injected in the later part of the inspiratory cycle, otherwise fibers already had deposited or left that airway generation. The deposition efficiency and the fraction of fibers that remained suspended at the end of the simulation are shown in Table 4 for fibers injected at $3/4 t_{in}$ in generation 16. The inclusion of the short pause after the inhalation resulted in slightly increased deposition for most cases. The distances covered by the fibers in the extra time given by the pause is quite small, however, and in earlier generations, where airway diameters are larger and the fraction of suspended fibers after an inhalation is smaller, only minor increase in deposition was obtained.

Fiber Transport During Zero-Flow in the Distal Airways. After the lobar bronchi, the velocity in the airways decreases rapidly as a result of the tremendous increase in total

airway cross-sectional area due to the large number of small airways [3]. Hence, very low velocities are found in the distal airways, and as an extension of the preceding discussion, deposition simulations are carried out for zero-flow over the time of the breathing pause, t_{pause} . The result is that the small and close to spherical nanoparticles ($d_f = 10$ nm, $\beta = 3$) are deposited to a rather large extent 23–39% while fibrous nanoparticles ($\beta = 100$) of the same diameter and the larger nano particles are much less efficiently deposited < 6%, implying an increased risk of reaching the alveoli, see the right most column in Table 5.

Let us now do some analysis to scrutinize these results. The net Brownian displacement in a given time can be estimated with the formulas

$$x_{\text{rms}}^2 = \langle x^2 \rangle = 2D't \quad (24)$$

$$r_{\text{rms}}^2 = \langle x^2 \rangle + \langle z^2 \rangle = 4D't \quad (25)$$

for 1D and 2D motion, respectively. Here the diffusion coefficient is averaged over all directions using

$$D' = \frac{1}{3} (2D'_{\perp} + D'_{\parallel}) \quad (26)$$

From Eq. (24), the time required for a fiber to diffuse through an airway of length L can be estimated with

$$t_{L}^{Br} = L^2 / (2D') \quad (27)$$

and the time to radially diffuse one airway diameter can similarly be estimated with

$$t_{D_{\text{pipe}}}^{Br} = D_{\text{pipe}}^2 / (4D') \quad (28)$$

The relative size of the net Brownian displacement in the radial direction during t_{pause} can be computed as

$$r_{\text{rms}}^{\text{pause}} / D_{\text{pipe}} \quad (29)$$

To connect the radial displacement to the DE of fibers released with uniform distribution over the airway entrance as done in the simulations, the quantity $r_{\text{rms}}^{\text{pause}} / D_{\text{pipe}}$ can be regarded as the maximum distance from an airway wall that a fiber may start from in order to deposit in an airway of a certain dimension within a given time. The deposition efficiency calculated in this way compares very well with those from the simulations (see Table 5). For the largest nanofibers considered ($d_f = 100$ nm, $\beta = 100$) interception adds to the deposition, which explains the discrepancy seen between analysis and simulation results for these fibers. The deposition efficiency without interception is shown in parenthesis, and again good agreement is obtained with theory. Thus when interception comes into play, Eq. (29) is not very useful, reflecting the usefulness of the simulations once the problem becomes a little bit more complex. The analysis furthermore yields that $t_{D_{\text{pipe}}}^{Br}$ is long or very long compared to t_{pause} , and that it rapidly increases with fiber size and aspect ratio, which explains the subsequent decrease in deposition efficiency. The time t_{L}^{Br} is even longer; thus the Brownian displacement in the airway length-wise direction is negligible. After sorting this out it is safe to conclude that, except for the spherical 10 nm-particles, the nanoparticles basically follow the streamlines and seem to have the potential to reach the last generations of the respiratory airways without being deposited to any larger extent along the way.

For comparison, we also performed deposition simulations for microfibers in the same airway generations. As opposed to the nanofibers, the deposition of microfibers increases with fiber aspect ratio for a given particle diameter due to the added contribution from sedimentation (due to larger particle mass) and interception (due to increased fiber length), and all but the shortest

Table 5 Nanoparticle deposition for zero-flow during t_{pause} and diffusion time-scales in the distal airways

Gen	$D_{\text{pipe}} [\text{mm}]$	$d_f [\mu\text{m}]$	β	$D' [\text{m}^2/\text{s}]$	$t_{D_{\text{pipe}}}^{\text{Br}} [\text{s}]$	$t_{L}^{\text{Br}} [\text{s}]$	$r_{\text{rms}}^{\text{pause}}/D_{\text{pipe}} (\%)$	DE (%)
16	0.60	0.01	3	$2.7 \cdot 10^{-8}$	3.3	50.5	24.5	23.5
			100	$9.7 \cdot 10^{-10}$	93	$1.4 \cdot 10^3$	4.6	4.5
			3	$3.7 \cdot 10^{-10}$	$2.4 \cdot 10^2$	$3.7 \cdot 10^3$	2.9	2.7
			100	$2.0 \cdot 10^{-11}$	$4.6 \cdot 10^3$	$6.9 \cdot 10^4$	0.7	1.9 (0.6)
19	0.47	0.01	3	As above	2.1	18.2	31.3	32.6
			100		57	$5.1 \cdot 10^2$	5.9	5.4
			3		$1.5 \cdot 10^2$	$1.3 \cdot 10^3$	3.7	3.1
			100		$2.8 \cdot 10^3$	$2.5 \cdot 10^4$	0.9	2.2 (0.7)
22	0.41	0.01	3	As above	1.6	6.5	35.8	39.1
			100		43	$1.8 \cdot 10^2$	6.8	6.2
			3		$1.1 \cdot 10^2$	$4.7 \cdot 10^3$	4.2	3.5
			100		$2.1 \cdot 10^3$	$8.8 \cdot 10^3$	1.0	2.5 (0.8)

Table 6 Microfiber deposition at zero-flow during t_{pause} in the distal airways

Gen	$D_{\text{pipe}} [\text{mm}]$	$d_f [\mu\text{m}]$	β	DE (%)
16	0.60	1.0	3	1.5
			100	10.0
			3	5.5
			100	35.5
19	0.47	1.0	3	28.4
			100	12.8
			3	7.9
			100	45.7
22	0.41	1.0	3	41.6
			100	14.6
			3	9.1
			100	51.1
		5.0	3	47.4

microfibers were experiencing significant deposition during the breathing pause (see Table 6).

Conclusions

Cyclic inhalation and deposition was examined for spherical and fibrous particles ranging from micro- to nanoscale. The influence of the breathing pattern on the fate of inhaled particles was studied. Maximum deposition is obtained when fibers are released at the start of the inspiratory cycle, and the minimum is received at the peak of inhalation. In general, quasi-steady solutions provide a good approximation to the cyclic flow if an appropriate mean velocity is used. This suggests that a steady state flow scheme can be used experimentally greatly simplifying the required experimental setup. It can furthermore be concluded, with high statistical significance, that for a batch type of supply of particles the deposition in one inhalation is higher at light activity than at heavy breathing. For a continuous supply of particles, however, the results suggest that the delivered dose is considerably higher for the higher activity level. The inclusion of a short pause after the inhalation results in an increased deposition in the terminal bronchiole; the distance covered by the fibers in the extra time given by the pause is quite small, however, and hence only minor effects were found in earlier airway generations. During zero-flow over the time of a breathing pause, the spherical 10 nm particles were experiencing significant deposition in the distal airways, whereas only a few percent of the larger and/or fibrous nanoparticles were deposited. The ratio of the net Brownian displacement in the radial direction during the time of the breathing

pause and the airway diameter is a good prediction of nanofiber deposition, except for very slender and long fibers; thus in most cases this can be regarded as the maximum distance from an airway wall that a fiber may start from in order to deposit in an airway of a certain dimension within a given time. For particles in the micro-range, all but the shortest microfibers were significantly deposited during a breathing pause.

Finally, for all the breathing parameters examined, the lowest deposition efficiency was obtained for spherical 1 μm -particles and fibrous 100 nm-particles. The former is expected from studies on spherical particles, for which deposition is known to be least efficient for particles with diameters around 0.5–1 μm , and the latter is in agreement with results in Högberg et al. [13] where it was found that for particles with elongated shape, minimum deposition is achieved for particles with diameters in the size range 10–100 nm and lengths of 1–10 μm . The latter includes a common size-range of Multi-walled carbon nanotubes.

The results presented here holds for straight tubes with smooth walls; in a parallel study we have found that the surface roughness in the form of cartilaginous rings present in the lower generations have a small effect on deposition of spherical nano-particles. Since nano-fibers in general give smaller deposition rates than spherical particles, we believe that this is also the case for fiber deposition with a wall structure like cartilaginous rings [29]. Ongoing work includes different forms of the particles [30] and more complex shapes of the air ways including secondary flows of different types [8,17,20].

Acknowledgment

The authors would like to acknowledge the Swedish Research Council and the Swedish Agency for Economic and Regional Growth for funding this work.

Appendix

The dimensions of the different airways of the Weibel geometry are listed in Table A1.

Table A1 Dimensions of the different airways of the Weibel geometry

Generation	Radius [mm]	Length [mm]
0	9	120
6	1.4	90
11	0.545	3.9
16	0.3	1.65
19	0.235	0.99
22	0.205	0.59

References

- [1] Sandstrom, T., Cassee, F. C., Salonen, R. O., and Dybing, E., 2005, "Recent Outcomes in European Multi-Centre Projects on Ambient Particulate Air Pollution," *Toxicol. Appl. Pharmacol.*, **1**(207, 2 Suppl), pp. 261–268.
- [2] Sandstrom, T., Nowak, D., and van Bree, L., 2005, "Health Effects of Coarse Particles in Ambient Air: Messages for Research and Decision-Making," *Eur. Respir. J.*, **26**(2), pp. 187–188.
- [3] Hinds, W. C., 1999, *Aerosol Technology: Properties, Behavior, and Measurement of Airborne Particles*, Wiley, New York.
- [4] Zhang, Z., Kleinstreuer, C., and Kim, C. S., 2001, "Flow Structure and Particle Transport in a Triple Bifurcation Airway Model," *Trans. ASME J. Fluids Eng.*, **123**(6), pp. 320–330.
- [5] Walters, D. K., and Luke, W. H., 2010, "A Method for Three-Dimensional Navier-Stokes Simulations of Large-Scale Regions of the Human Lung Airway," *Trans. ASME J. Fluids Eng.*, **132**(5), pp. 511011–511018.
- [6] Kleinstreuer, C., and Zhang, Z., 2010, "Airflow and Particle Transport in the Human Respiratory System," *Annu. Rev. Fluid Mech.*, **42**(1), pp. 301–34.
- [7] Zhang, Z., Kleinstreuer, C., and Kim, C. S., 2002, "Cyclic Micron-Size Particle Inhalation and Deposition in a Triple Bifurcation Lung Airway Model," *J. Aerosol. Sci.*, **33**, pp. 257–281.
- [8] Kim, C. S., and Fisher, D. M., 1999, "Deposition Characteristics of Aerosol Particles in Sequentially Bifurcating Airway Models," *Aerosol Sci. Technol.*, **31**, pp. 198–220.
- [9] Zhang, Z., and Kleinstreuer, C., and Kim, C. S., 2004, "Airflow Structures and Nano-particle Deposition in a Human Upper Airway Model," *J. Comput. Phys.*, **198**, pp. 178–201.
- [10] Myojo, T., 1997, "Deposition of Fibrous Aerosol in a Model of a Human Lung Bifurcation Under Cyclic Flow Conditions," *Ann. Occup. Hyg.*, **41**(1), pp. 142–147.
- [11] Kojic, M., and Tsuda, A., 2004, "A Simple Model for Gravitational Deposition of Non-diffusing Particles in Oscillating Laminar Pipe Flow and its Applications to Small Airways," *J. Aerosol Sci.*, **35**, pp. 245–261.
- [12] Saffman, P. G., 1965, "The Lift on a Small Sphere in a Slow Shear Flow," *J. Fluid Mech.*, **22**, pp. 385–400.
- [13] Högberg, S. M., Åkerstedt, H. O., Lundstrom, T. S., and Freund, J. F., 2010, "Respiratory Deposition of Fibers in the Non-inertial Regime—Development and Application of a Semi-Analytical Model," *Aerosol Sci. Technol.*, **44**, pp. 847–860.
- [14] Högberg, S. M., and Lundstrom, T. S., (2011), "Motion of Dispersed Carbon Nanotubes during Impregnation of Fabrics," *Plast. Rubber Compos.: Macromol. Eng.*, **40**(2), pp. 70–79.
- [15] Pich, J., 1972, "Theory of Gravitational Deposition of Particles from Laminar Flows in Channels," *J. Aerosol Sci.*, **3**, pp. 351–361.
- [16] Ingham, D. B., 1975, "Diffusion of Aerosols from a Stream Flowing through a Cylindrical Tube," *J. Aerosol Sci.*, **6**, pp. 125–132.
- [17] Åkerstedt, H. O., Högberg, S. M., and Lundstrom, T. S., 2012, "An Asymptotic Approach of Brownian Deposition of Nanofibers in Pipe Flow," *Theor. Comput. Fluid Dyn.*, (to be published).
- [18] Shimizu, Y., Futaki, Y., and Martin, C. S., 1992, "Secondary Flow and Hydraulic Losses within Sinuous Conduits of Rectangular Cross Section," *Trans. ASME J. Fluids Eng.*, **114**, pp. 593–600.
- [19] Liou, T.-M., Chen, C.-C., and Chen, M.-Y., 2003, "Rotating Effect on Fluid Flow in Two Smooth Ducts Connected by a 180-Degree Bend," *Trans. ASME J. Fluids Eng.*, **125**, pp. 138–148.
- [20] Larsson, I. A. S., Lindmark, E. M., Lundstrom, T. S., and Nathan, J. G., 2011, "Secondary Flow in Semi Circular Ducts," *Trans. ASME J. Fluids Eng.*, **133**(10), p. 101206.
- [21] Finlay, W. H., 2001, *The Mechanics of Inhaled Pharmaceutical Aerosols*, Academic Press, London.
- [22] Schlichting, H., and Gersten, K., 2000, *Boundary-Layer Theory*, Springer, Berlin.
- [23] Goldstein, H., 1980, *Classical Mechanics*, 2nd ed., Addison-Wesley, Reading, MA.
- [24] Rapaport, D. C., 1997, *The Art of Molecular Dynamics Simulation*, Cambridge University Press, Cambridge, UK.
- [25] Weibel, E. R., 1963, *Morphometry of the Human Lung*, Academic Press, New York.
- [26] ICRP Task Group on Lung Dynamics, 1966, "Deposition and Retention Models for Internal Dosimetry of the Human Respiratory Tract," *Health. Phys.*, **12**, pp. 173–207.
- [27] Bull, J. L., 2007, "The Application of Microbubbles for Targeted Drug Delivery," *Expert Opin. Drug Deliv.*, **4**, pp. 475–493.
- [28] Marjavaara, B. D., Lundstrom, T. S., Goel, T., Mack, Y., and Shyy, W., 2007, "Hydraulic Diffuser Shape Optimisation by Multiple Surrogate Model Approximations of Pareto Fronts," *Trans. ASME J. Fluids Eng.*, **129**(9), pp. 1228–1240.
- [29] Åkerstedt, H. O., Högberg, S. M., Lundstrom, T. S., and Sandstrom, T., 2010, "The Effect of Cartilaginous Rings on Particle Deposition by Convection and Brownian Diffusion," *Nat. Sci.*, **2**(7), pp. 769–779.
- [30] Scheckman, J. H., and McMurphy, P. H., 2011, "Deposition of Silica Agglomerates in a Cast of Human Lung Airways: Enhancement Relative to Spheres of Equal Mobility and Aerodynamic Diameter," *J. Aerosol Sci.*, **42**(8), pp. 508–516.

Modelling transport and deposition
rate of oblate and prolate nano-
and micro particles in a virtual
model of the human airway

Authors:

Elise Holmstedt, Hans O. Åkerstedt, T. Staffan Lundström

Submitted to Journal of Fluids Engineering

Modelling transport and deposition rate of oblate and prolate nano- and micro particles in a virtual model of the human airway

Elise Holmstedt, Hans O. Åkerstedt, T. Staffan Lundström

Division of Fluid and Experimental Mechanics, Luleå University of Technology,
SE-971 87 Luleå, Sweden

Abstract

A model for the motion of oblate and prolate spheroids in the nano- and micro scale was developed. The aim was to mimic the environment of the human lung and the deposition of fibres during inhalation, but the model is, in itself, general and can be applied for different flows and geometries for small fibre Stokes and Reynolds numbers. The initial condition is an evenly random distribution of particles and the model is, in this case, used to follow them in a steady, laminar, fully developed parabolic flow in a straight airway. The effect of gravitational settling and Brownian motion was included and the particle was said to be deposited when its centre of mass moved outside the wall of the bronchi.

A statistical study was done comparing the deposition rates of oblate and prolate spheroids of different size and aspect ratio as they travel down the narrowing bronchi. The numerical simulations based on the model show a clear correlation between increased depositions with increase of the particle size and yielded a higher deposition for oblate spheroids as compared to prolate spheroids with the same aspect ratio.

A study of the motion and orientation of a single oblate and prolate particle has also been done. For micro particles the motion of the particles was only influenced by the flow field and Jeffery orbits were clearly visible. This behaviour was observed for both oblate and prolate particles. For nano particles that are influenced by Brownian motion the overall behaviour of the prolate spheroids remained mainly the same. The behaviour of the oblate particles on the other hand was greatly changed to a seemingly random tumbling behaviour.

1 Introduction

Theories for the motion of oblate and prolate ellipsoids will be outlined and the models presented will be applied on particle deposition in the respiratory airways. The theory is important for a number of applications including particle deposition in the respiratory airway [1, 2], the feeding of bio-fuels [3, 4], the manufacturing of fibre reinforced composites with added properties [5, 6] and paper making [7, 8]. Regarding particle deposition in the respiratory airways the topic is significant both for evaluating health effects of inhaled toxic matter and for estimating the efficacy of drug delivery with pharmaceutical aerosols [9, 10, 11].

The development of new smart materials containing micro and nano-particles, such as carbon nano-tubes, is a very popular branch of material science nowadays. Such tiny and non-spherical particles are, however, potentially toxic and thus may pose a substantial health risk [12]. Carbon nano-tubes are approximately 10–100 nm in diameter with lengths of around 1–50 μm and can be treated as prolate ellipsoids. Although usually smaller than asbestos fibres, there are concerns that they may cause similar adverse health effects upon inhalation. Nano-particles may be given additional shapes like oblate ellipsoids, [13]. This is a shape that also may describe wood chips and micro-particles for drug-delivery [14]. Hence there are many reasons to do fundamental studies of the motion of prolate and oblate ellipsoids [15, 16].

There are two main techniques for the analysis of the transport of particles and their deposition for a given flow and geometry. One method is to solve the particle equations of motion for a flow field given by the solution of the Navier-Stokes equations. To include effects of Brownian motion then a stochastic force is introduced. If launching a large number N of particles, particle deposition statistics can be disclosed, and the error of the method is $O(N^{1/2})$. This method has been successfully applied to derive the deposition of micro- and nano-prolate particles for a fully developed pipe flow [17]. The second approach is to utilize the Fokker-Planck equation, which has the advantage of directly providing the statistical averages [18]. This method has, for instance, been used to study the deposition of spherical and non-spherical nano-particles in a model airway with cartilaginous rings, representing the large conducting airways [19, 20]. The Fokker-Planck equation for non-spherical particles was considered for fully developed pipe flow by Asgharian et al. [21].

2 Simulation set-up

A steady laminar fully developed parabolic flow field is assumed to move in the positive y -direction in a cylindrical pipe with the inlet in the $y = 0$ plane. A representation of the geometry can be seen in Figure 1. In this figure the initial positions of an oblate and prolate particle in a single particle simulation are also defined. Two types of geometries will be considered, a pipe with uniform cross-section to study the evaluation of orientation of single particles and a pipe with a, in steps, narrowing cross-section to mimic the human airways and thus enabling a study of deposition rates as a function of position in the lung.

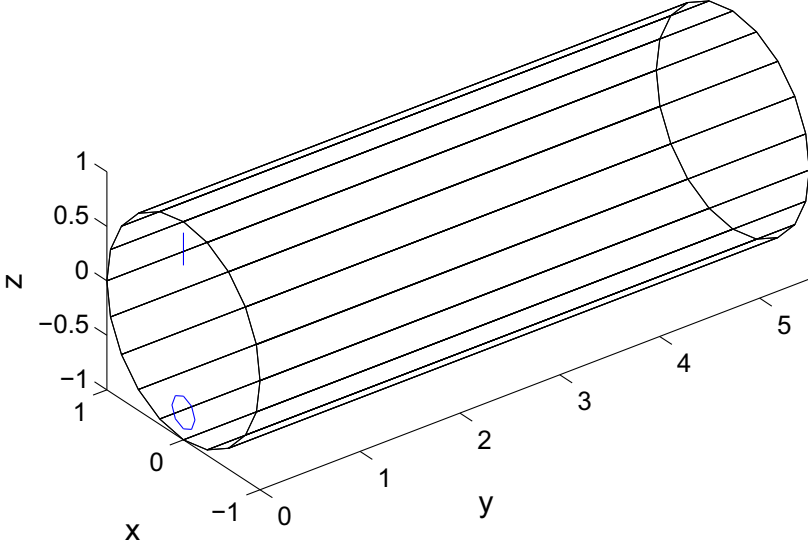


Figure 1: A representative sketch of the geometry used in the simulations with the initial position for an oblate and a prolate particle in the single particle runs.

2.1 Fibre equations of motion

Two coordinate systems are defined to describe the movement of the particles. Global coordinates $[x, y, z]$, and local ones $[x', y', z']$ fixed to the particle with the polar axis along z' . The global coordinate system has the inlet of the airway on the $[x, z]$ plane with origin fixed in the centre of the circular inlet and the flow field moving in the positive y direction. A particles rotate, the angle between the local and global coordinates, is described using Euler angles, depicted in Figure 2.

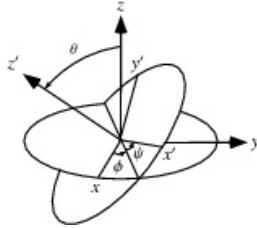


Figure 2: Euler angles connecting a particles local coordinates to the global ones [5].

For this study, with small Stokes numbers (St) for the particles, inertia may be neglected and the fibre equations of motion are reduced to

$$F_i^h + F_i^g + f_i^{Br} = 0 \quad (1)$$

$$T_{i'}^h + T_{i'}^{Br} = 0 \quad (2)$$

in which F_i^h , F_i^g and F_i^{Br} are the hydrodynamic, gravitational and Brownian forces and $T_{i'}^h$ and $T_{i'}^{Br}$ are the hydrodynamic and Brownian torques.

2.2 Hydrodynamic force and torque

The drag force on the particles considered in this study may be expressed as

$$\mathbf{F}^h = 3\pi\mu\mathbf{A}^T \begin{bmatrix} d_{\perp} & 0 & 0 \\ 0 & d_{\perp} & 0 \\ 0 & 0 & d_{\parallel} \end{bmatrix} \mathbf{A} \begin{bmatrix} u - \frac{dx}{dt} \\ v - \frac{dy}{dt} \\ w - \frac{dz}{dt} \end{bmatrix} \quad (3)$$

and is thus dependent on the orientation of the particle in the stokes flow regime. In this equation μ is the dynamic viscosity of the fluid, $[u, v, w]$ are the components of the fluid velocity, $[\frac{dx}{dt}, \frac{dy}{dt}, \frac{dz}{dt}]$ the components of the particle velocities and \mathbf{A} is the rotation matrix between the local and global coordinates.

2.2.1 Translation

For a prolate spheroid d_{\perp} and d_{\parallel} are the Stokes parameters oriented perpendicular and parallel to the direction of motion, respectively [17], and are given by:

$$\frac{d_{\perp}}{d_f} = \frac{\frac{8}{3}(\beta^2 - 1)}{C_{\perp}^t \left[\frac{2\beta^2 - 3}{\sqrt{\beta^2 - 1}} \ln(\beta + \sqrt{\beta^2 - 1}) + \beta \right]} \quad (4)$$

$$\frac{d_{\parallel}}{d_f} = \frac{\frac{4}{3}(\beta^2 - 1)}{C_{\parallel}^t \left[\frac{2\beta^2 - 3}{\sqrt{\beta^2 - 1}} \ln(\beta + \sqrt{\beta^2 - 1}) - \beta \right]}. \quad (5)$$

Here β and d_f are the fibre aspect ratio and geometric diameter respectively, C_{\parallel}^t and C_{\perp}^t are the slip correction factors for the fluid dynamic drag that are included to extend the validity of the drag force to include particles that are so small that their diameter is close to the mean free drag of air molecules.

To obtain the corresponding expressions for oblate spheroids the replacement $\beta \rightarrow 1/\beta$ is introduced in (4) and (5) so that the aspect ratio β is greater than unity for prolate and oblate spheroids. The Stokes parameters for oblate spheroids are then given by

$$\frac{d_{\perp}}{d_f} = \frac{\frac{8}{3}(\beta^2 - 1)}{C_{\perp}^t \left[\frac{\beta(3\beta^2 - 2)}{\sqrt{\beta^2 - 1}} \arctan(\sqrt{\beta^2 - 1}) \right]} \quad (6)$$

$$\frac{d_{\parallel}}{d_f} = \frac{\frac{4}{3}(\beta^2 - 1)}{C_{\parallel}^t \left[\frac{\beta(\beta^2 - 2)}{\sqrt{\beta^2 - 1}} \arctan(\sqrt{\beta^2 - 1}) \right]} \quad (7)$$

No exact expression for the slip correction factors exists for prolate and oblate spheroids and an approximate method by Dahneke [22] is applied. This method will be outlined in section 2.2.3.

2.2.2 Rotation

The equations for the fluid dynamic torque for an ellipsoid body in a viscous shear flow as derived by Jeffery [23] and simplified for the current case can be written in the following manner

$$T_{x'}^h = \frac{1}{N_{\perp}^r} \left[(\xi' - \omega_{x'}) - \left(\frac{\beta^2 - 1}{\beta^2 + 1} \right) \dot{\epsilon}_{y'z'} \right], \quad (8)$$

$$T_{y'}^h = \frac{1}{N_{\perp}^r} \left[(\eta' - \omega_{y'}) - \left(\frac{\beta^2 - 1}{\beta^2 + 1} \right) \dot{\epsilon}_{x'z'} \right]. \quad (9)$$

Due to rotational symmetry rotation about the major axis does not affect the transport and is therefore omitted. The tensor $\omega_{i'}$ is the fibre angular velocity, $\dot{\epsilon}_{ij} = \frac{1}{2} \left(\frac{\partial u_j}{\partial x_i} + \frac{\partial u_i}{\partial x_j} \right)$ is the elements of the deformation rate and $[\xi, \eta, \zeta]^T = \frac{1}{2}(\nabla \times \mathbf{u})$ is the spin tensor. The latter two tensors are derived from the global flow field and are translated to local equivalents by

$$\dot{\epsilon}_{i'j'} = \mathbf{A} \dot{\epsilon}_{ij} \mathbf{A}^T, \quad (10)$$

$$[\xi', \eta', \zeta']^T = \mathbf{A}[\xi, \eta, \zeta]^T. \quad (11)$$

The angular mobility for prolate spheroids may be expressed as [17]

$$B_{\perp}^r = \frac{3C_{\perp}^r \left[\frac{2\beta^2-1}{\sqrt{\beta^2-1}} \ln(\beta + \sqrt{\beta^2-1}) - \beta \right]}{2\pi\mu d_f^3(\beta^4-1)}. \quad (12)$$

For oblate spheroids this mobility is given by the following relationship

$$B_{\perp}^r = \frac{3C_{\perp}^r \left[\frac{(2-\beta^2)\beta}{\sqrt{\beta^2-1}} \arctan(\sqrt{\beta^2-1}) - \beta \right]}{2\pi\mu d_f^3(\frac{1}{\beta^2} - \beta^2)}. \quad (13)$$

2.2.3 Slip corrections factors

No exact expressions for the drag of prolate and oblate spheroids exist in the free molecular flow limit $\text{Kn} = \frac{2\lambda}{d_f} \rightarrow \infty$ where λ is the mean free path of the air molecules. For cylinders however expressions have been derived by Dahneke [24]. Therefore in this limit the drag of prolate and oblate spheroids are modelled by the results of a cylinder. To extended the validity for the drag force from small Knudsen numbers Kn to large Kn the Cunningham factors are applied with an adjusted radii as suggested by Dahneke [24]. The Cunningham factors for prolate spheroids are given by Högberg et al [17]. Using the replacement $\beta \rightarrow 1/\beta$ gives the following result for oblate spheroids

$$C_{i'} = 1 + \frac{d_f}{2r_{i'}} \text{Kn} \left[1.257 + 0.4 \exp \left(\frac{-2.2r_{i'}}{d_f \text{Kn}} \right) \right]$$

The adjusted radii for translational motion parallel and perpendicular to

the flow are then expressed as

$$\begin{aligned}
r_1 &= \frac{1.657d_f\beta}{16(\beta^2 - 1)} \\
\Lambda_1 &= \frac{1}{\sqrt{\beta^2 - 1}} \\
\Lambda_3 &= \Lambda_1 \log\left(\beta + \frac{1}{\Lambda_1}\right) \\
\Lambda_2 &= \beta - \Lambda_3 \\
r_\perp^t &= \frac{r_1}{2} \left[\frac{3\beta^2 + 4}{\sqrt{\beta^2 - 1}} \arctan \sqrt{\beta^2 - 1} - 1 \right] \times \\
&\quad \left[\Lambda_1^2 \Lambda_2 \left\{ \frac{(6 - \pi)}{4} f - 2 \right\} + \Lambda_3 \left\{ 4 - \frac{4 - \pi}{2} f \right\} + \frac{f}{\beta} \right] \\
r_\parallel^t &= r_1 \left[\frac{2\beta^2 - 1}{\sqrt{\beta^2 - 1}} \arctan \sqrt{\beta^2 - 1} + 1 \right] \times \\
&\quad \left[\Lambda_1^2 \Lambda_2 \left\{ 4 - \frac{(6 - \pi)}{2} f \right\} \beta^{-2} + \Lambda_3 f + \frac{f}{\beta} \right].
\end{aligned}$$

An adjusted radii for rotational movement of oblate spheroids around its axis is given by

$$\begin{aligned}
r_\perp^r &= \frac{1.675d_f}{\beta} \frac{3}{2} \left[\frac{\frac{(2-\beta^2)*\beta}{\sqrt{\beta^2-1}} \arctan(\sqrt{\beta^2-1}) - \beta}{\frac{1}{\beta^2} - \beta^2} \right] \times \\
&\quad \left[\frac{1}{4} + \frac{2\beta}{4} + \frac{(2\beta)^2}{4} + \frac{(2\beta)^3}{8} + f \left(\frac{\pi - 6}{48} - \frac{2\beta}{8} - \frac{(2\beta)^2}{8} + \frac{(\pi - 4)(2\beta)^3}{64} \right) \right].
\end{aligned}$$

2.3 Gravitational settling

One deposition mechanism is gravitational settling or sedimentation. It comes into play for large particle masses for longer time periods and is most noticeable within horizontal small airways. Particle density is usually much greater than the surrounding air and thus buoyancy can be neglected. The gravitational force is defined in the positive z -direction with magnitude

$$F_z^g = \pi \rho_f g d_f^3 \beta / 6, \quad (14)$$

where ρ_f is the density of the particle and g is the gravitational acceleration.

2.4 Brownian motion

The brownian force and torque are modelled as independent zero-mean Gaussian white-noise processes [17], which for spheroids take the following form

$$F_{i'}^{Br}(t) = \chi_{i'}^t \sqrt{\frac{\pi S_{i'}^t}{\delta t}}, \quad (15)$$

$$T_{i'}^{Br}(t) = \chi_{i'}^r \sqrt{\frac{\pi S_{i'}^r}{\delta t}}, \quad (16)$$

where $\chi_{i'}^t$ and $\chi_{i'}^r$ are standard normally distributed random numbers and δt is a Brownian time increment. The spectral intensities $S_{i'}^t$ and $S_{i'}^r$ are given by

$$S_{i'}^t = \frac{2\sigma T}{\pi} \frac{1}{B_{i'}^t}, \quad (17)$$

$$S_{i'}^r = \frac{2\sigma T}{\pi} \frac{1}{B_{i'}^r}, \quad (18)$$

in which σ is the Boltzmann constant and T is the absolute temperature. $B_{i'}^r$ is given in (12) and (13) and

$$B_{i'}^t = 3\pi\mu d_{i'}. \quad (19)$$

2.5 Numerical set-up for simulation of deposition rates in human airways

Lungs can be seen as pipes divided into smaller pipes that in turn are divided into even smaller pipes, etc. Each of these divisions is called a generation. The simulations are set-up here to start at the second generation, where it is reasonable to assume that the flow is laminar. Using Weibel's model [25] it is furthermore assumed that pipes in this generation are 19 mm long and have a diameter of 4.15 mm. The simulations are performed down to the 16th generation where the radius of the pipes is assumed to be 0.2 mm and the length 1.65 mm, [25]. The tracheal flow rate was 431 cm³/s corresponding to a tidal volume of 750 ml with an air temperature of 310 K and the particles have unit density. The model is currently set up and focused on the straight bronchi, not the intersections. Disturbances in the flow at the intersections are mainly driven by inertia and are therefore more important for higher Re than considered in this study. Secondary flow that can be induced in the

interceptions and a partly developing flow at one side of the pipe after the intersection is therefore neglected in the current set-up.

The purpose of the present work is to extend the methodology developed in Högberg et al. [17] for prolates to oblates and to compare the behaviour of these two shapes on the deposition rate in the human lung.

Simulations are thus run with 10000 particles with a density of 1000 kg/m³ for each combination of aspect ratio and geometric diameter and the deposition rate is calculated by observing how many particles are intercepted by the walls of the lungs and to the number of particles in the set.

2.6 Numerical set-up for single particle study

To be able to properly observe the Jeffery orbits made by a single particle it is necessary to follow the particle for a longer distance than for the airway model used in the multi-particle deposition simulations. In simulations of non-Brownian motion the diameter of the airway has no impact on the resulting Jeffery orbits and for the following examples generation 4 was chosen.

The geometric diameter of the particles has no impact on non-Brownian motion, but has a large impact on Brownian movement as it is, by its nature, a force that affects small particles. Therefore a relatively large particle with $d_f = 1 \mu\text{m}$ was chosen so the impact of Brownian motion can be observed but it is not the dominating force acting on the particles.

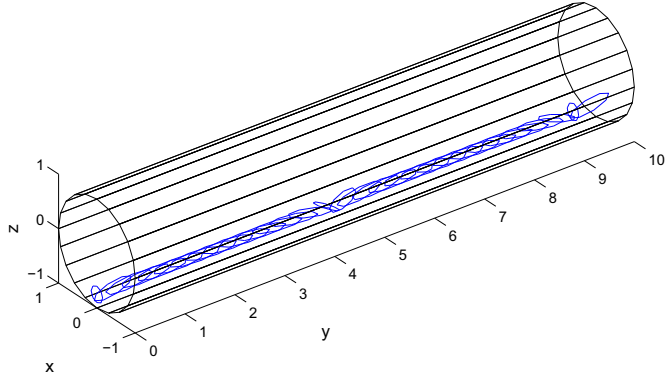
The placement of both oblate and prolate particles at the beginning of the simulations is such that the large surface of the particle is facing the flow as seen in Figure 1. For prolate particles this implies that the particle is directed perpendicular to the flow with $\theta = 90^\circ$ since its z' axis is directed along the length of the particle. Oblate particles are placed parallel to the flow with $\theta = 0^\circ$ since its z' axis is perpendicular to the surface of the particle. The angle ϕ describes the tilt of the particles z' axis from the global z axis, see Figure 2. The particles initial position is such that $\phi = 0^\circ$ and thus the pressure gradient over the particles on the horizontal plane is zero. The larger distance between the centre of the airway and the particles initial position, the slower the particle will move, and thus, experiences more Jeffery orbits. In these simulation the initial position was at a distance of $0.7r$ from the centre where r is the radius of the airway.

3 Results and Discussions

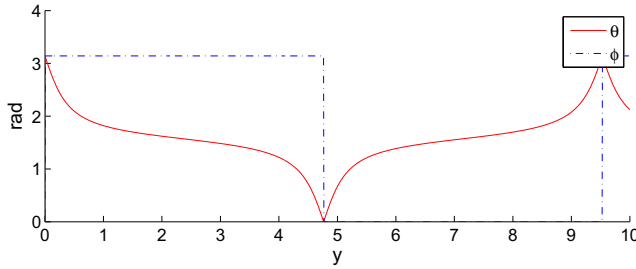
To elucidate the motion of oblate and prolate spheroids in human airways it is necessary to both scrutinize the detailed motion of a single particle and the accumulated results of a large number of particles.

3.1 Following one particle

Oblate and prolate spheroids are first studied for the case when they are only influenced by the flow field within the airways, discarding both Brownian motion and gravitational settling.

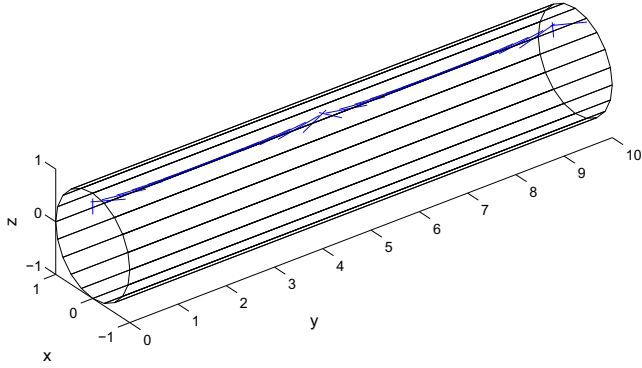


(a) The rotation of one oblate particle plotted at regular intervals as it moves through an airway.

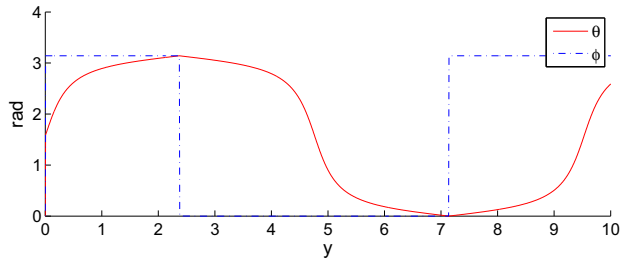


(b) The angles, θ and ϕ , describing the rotation of the oblate particle.

Figure 3: Description of the motion of an oblate spheroid with $d_f = 1 \mu\text{m}$, $\beta = 5$ and in an airway of generation 4.



(a) The rotation of one prolate particle plotted at regular intervals as it moves through an airway.



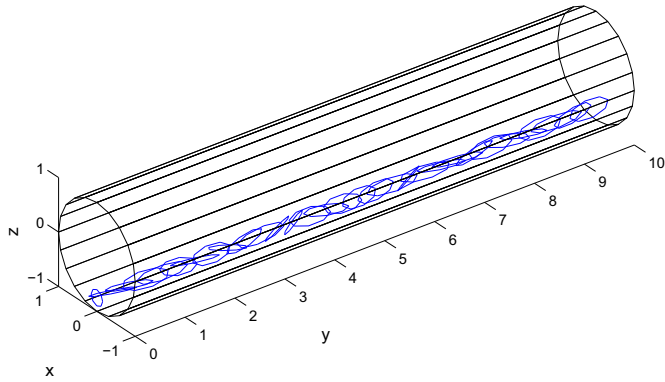
(b) The angles, θ and ϕ , describing the rotation of the prolate particle.

Figure 4: Description of the motion of a prolate spheroid with $d_f = 1 \mu\text{m}$, $\beta = 5$ and in an airway of generation 4.

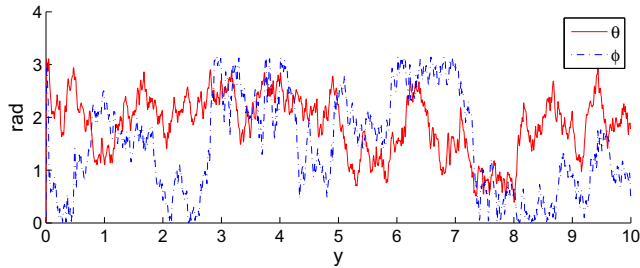
Both oblate and prolate spheroids exhibit a similar behaviour with Jeffery orbits appearing at the same interval, which can be seen in Figures 3a and 4a. In Figures 3b and 4b the particles Euler angles θ and ϕ can be seen. Since θ denotes the angle between the z' axis of the particle and the z axis of the flow it changes 180° during a Jeffery orbit in a characteristic manner, quickly around positions perpendicular to the flow and slowly otherwise. The angle ϕ describes the rotational angle around the flow; i.e. if the particle is pointing up, down or to the sides but since there are no horizontal forces acting on the particle this angle is unchanged until halfway through a Jeffery orbit when it switches 180° instantaneously when the side that previously faced 'up' now faces 'down'. Note that the size of the particles in the plots

are greatly exaggerated for the sake of clarity.

When Brownian motion is included the motion of the prolate and oblate particles becomes more irregular. For the prolate spheroids, although a randomized behaviour is obvious, Jeffery orbits are still visible, but with a shorter and not as regular periodicity, see Figure 6a. The behaviour of the oblate spheroids are less regular without any Jeffery orbits, see Figure 5a. It is also obvious that Brownian motion influences ϕ for both types of particles but much more for the oblate spheroids. This indicates that the motion of the oblate spheroids is much more sensitive to disturbances.

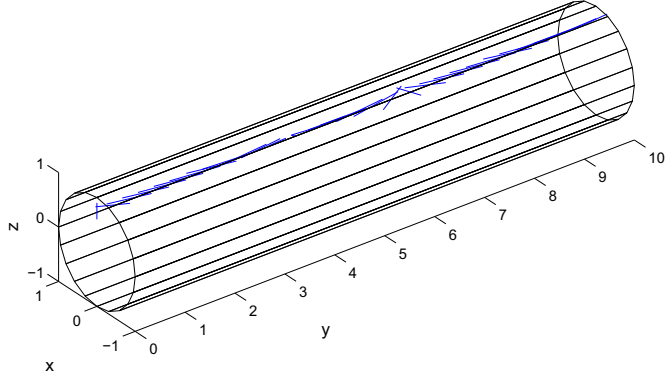


(a) Snapshots of an oblate particle as it moves through the airway.

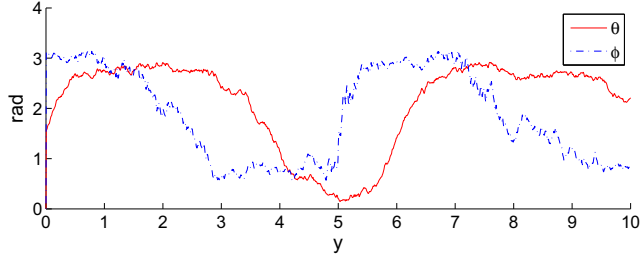


(b) The angular positions of an oblate particle

Figure 5: Similar setup as in Fig: 3 but with Brownian motion included.



(a) Snapshots of a prolate particle as it moves through the airway.



(b) The angular positions of a prolate particle

Figure 6: Similar setup as in Fig: 4 but with Brownian motion included.

3.2 Statistical deposition rates

During multiple particle simulations 10000 randomly distributed particles are launched and followed and their position of exit saved. Either the particles exited through the outlet or they are intercepted by the wall. The deposition rate is then calculated as the number of particles intercepting the wall to the number of particles launched at the inlet. To get a clear picture on how the different parameters influences the deposition rate, two main cases were studied. First the geometric diameter was changed and the aspect ratio kept constant. In the second case the influence of the aspect ratio β is in focus by varying it for a few different diameters of the particles. The influence of gravity is modelled in nearly all of the results here presented.

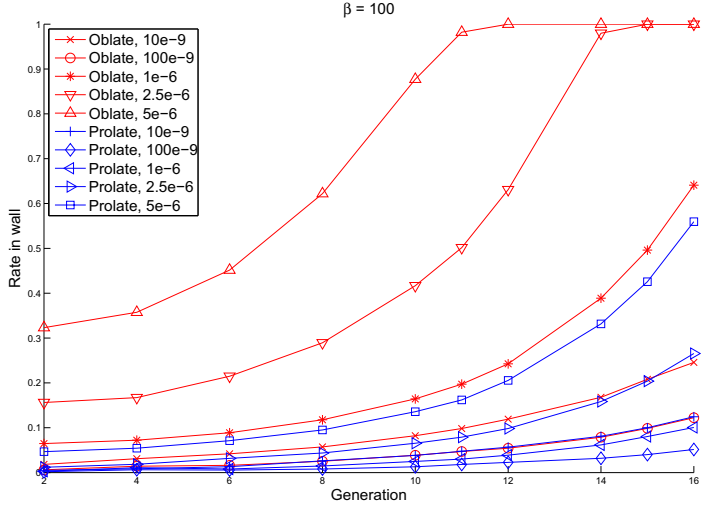
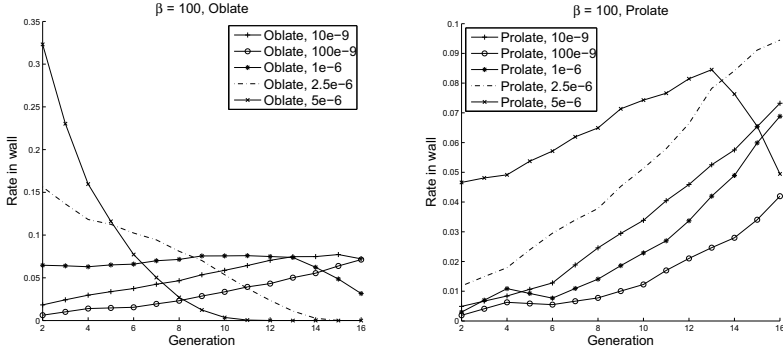


Figure 7: Simulations of particles with varied geometric diameter but with a fixed aspect ratio of $\beta = 100$.

3.2.1 Changing the geometric diameter

With $\beta = 100$ there is a correlation between deposition rates and particle size; when the particle size increases so does the deposition rate, except for the case with the smallest particles with a diameter of 10 nm where the deposition rates increase both in the oblate and prolate case due to the greater influence of the Brownian diffusion. It is also clear that the deposition rates for oblate spheroids are much greater than those of prolate spheroids and eventually they reach 100% deposition for the small airways. All this is seen in Figure 7 where the deposition rate is shown. Each curve shows the deposition rate for particles of different geometric diameter d_f , both oblate and prolate.

The results can also be plotted as a cumulative deposition in a model from generation 2 to 16, where the deposition in the inner generations are dependent on the deposition in the generations above. In this model it is easy to distinguish in which generation most fibres are being deposited, as displayed in Figures 8a and 8b where the deposition rates for oblate and prolate spheroids have been plotted respectively. Larger oblate spheroid are being deposited higher up in the airway while smaller particles have a quite even distribution. For prolate particles it is clear that the majority of the



(a) Cumulative deposition of oblate spheroids. (b) Cumulative deposition of prolate spheroids.

Figure 8: Deposition rates for each generation as particles passes through the complete model of the lung.

particles are being deposited in the smallest bronchi.

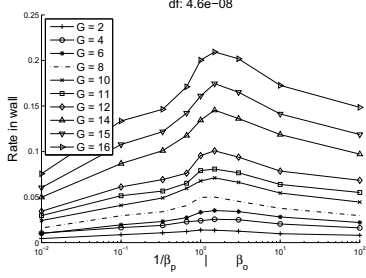
3.2.2 Changing the aspect ratio

To make the results for these simulations clearer the results from the simulations of the prolate particles deposition rate are plotted against the inverse of their β value on the x-axis on a logarithmic scale. Each line represents the deposition in each generation of bronchi with the prolate particles on the left hand side, the oblate particles on the right and a particle with an aspect ratio of $\beta = 1$ in the middle.

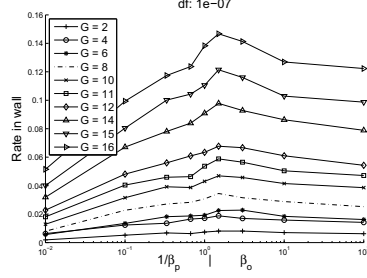
As is seen in Figure 9a the maximum deposition is not achieved for a sphere but for an oblate particle with aspect ratio of about $\beta = 1.5$. It should, however, be noted that since the slip correction factors for very small oblate spheroids are an approximation based on the formula for a cylinder instead of a spheroid the results where the aspect ratio is close to one may be susceptible to modelling errors, which may be one reason for this behaviour.

To see the effect of the aspect ratio on the deposition rates of particles a number of simulations were carried out with a fixed geometric diameter and an aspect ratio that goes from a prolate particle with $\beta_p = 100$ down to $\beta = 1$, and then up to $\beta_o = 100$ for oblate particles, see Figure 9.

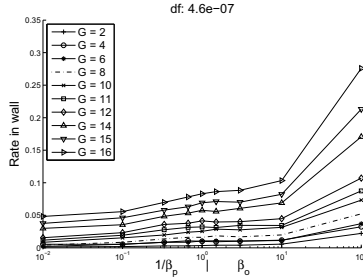
Observing the results for the deposition for particles of size $d_f = 46$ nm it is clear that the particles with a lower aspect ratio have a higher deposition rate both for oblate and prolate spheroids suggesting that an increase in β



(a) Geometric diameter of $460\mu\text{m}$.



(b) Geometric diameter of $10\mu\text{m}$.



(c) Geometric diameter of $46\mu\text{m}$.

Figure 9: Simulations of depositions of particles with changed aspect ratio. Plotted on a logarithmic scale with the inverse of β for the prolate particles.

stabilizes the motion of the particles, as can be observed in Figure 9a.

Once the particles get larger this behaviour can be observed to change. Studying Figure 9b, deposition rates for particles with a geometric diameter of $d_f = 100$ nm starts increasing for oblate spheroids compared to prolate spheroids. At around particle size of $d_f = 460$ nm the behaviour of the oblate spheroids becomes inverted and the largest deposition is now taking place for the largest aspect ratios as seen in Figure 9c. At the particle size of $d_f = 1 \mu\text{m}$ this behaviour starts appearing for prolate particles. A comparison to simulations carried out without the gravitational force yields that most of this behaviour arises from the increasing influence gravity has on the heavier particles.

4 Conclusions

A semi-analytical model describing the motion of oblate and prolate spheroids on the nano and micro scales has been developed, and simulations enabling both single particle tracking and aggregation of multiple particle deposition were carried out. In this work the focus was on particle movement and deposition in bronchi, but the model can be applied to a variety of cases with small particle Reynolds and Stokes numbers including more advanced models of the geometry of the human lung [26].

It is clear from the simulations that the shape of the particles greatly influences the deposition of said particles. It is well known that reduced particle size reduces the gravitational sedimentation but increases the Brownian diffusion, which corresponds to the results from this model. What the model has shown is how great each of those effects have on the particles and also how different shapes are affected differently. There is a clear connection between a reduction in deposition rate and a reduced particle diameter meaning a reduction of the effect of gravitational sedimentation. There is also an increase in deposition for the very small particles where the Brownian diffusion starts to have a noticeable effect. A consistent result is also a much higher deposition rate for oblate spheroids as compared to prolate spheroids. This behaviour can be traced back to the greater influence the Brownian forces have on them. There was also a noticeable influence on the results from changing the aspect ratios of the particles. The deposition rates for the smallest particles was the lowest for both the oblate and prolate spheroids with the highest aspect ratio, but interestingly enough the peak deposition was not for the spherical particles but for those who were slightly oblate with an aspect ratio of about 1.5, however, this might be a modelling error since the small oblate particles are approximated as a cylinder, not a sphere. For particles in the micro scale this behaviour was inverse and the highest deposition was found with the highest aspect ratios. By running simulations without gravitational forces acting on the particles this behaviour is concluded to be influenced by sedimentation effects. Thus smaller prolate spheroids will get the deepest into the lungs while oblate spheroids will be intercepted in the larger bronchi.

The stability of the path of the particle is shown to be greatly dependent on particle shape and size. Particles that are only influenced by the flow field will display clear Jeffery orbits, whose frequency is only set by the particle aspect ratio and where in the flow field the particle is moving. When the particles are under the influence of Brownian forces this behaviour is changed and particle type and size becomes important. Prolate micro-particles still display distinguishable Jeffery orbits while oblate particles of the same size

do not, indicating that their rotational position is much less stable. Nano-particles of both types did not have distinguishable Jeffery orbits since the Brownian forces acting on them were too great.

5 Acknowledgement

The authors would like to thank the Swedish Research Council for funding this work.

References

- [1] Z. Zhang, C. Kleinstreuer, and C. S. Kim J. Flow structure and particle transport in a triple bifurcation airway model. *Fluids Eng.*, 123(2):320–330, 2000.
- [2] S.M Högberg, H.O. Åkerstedt, E. Holmstedt, T.S. Lundström, and T Sandström. Time-dependent deposition of micro- and nanofibers in straight model airways. *Journal of Fluids Engineering, Trans. ASME J. Fluids Eng*, 134(5), 2012.
- [3] Svoboda, Karel, Pohorely, Michael, Hartman, and Miloslav. Pretreatment and feeding of biomass for pressurized entrained flow gasification. *FUEL PROCESSING TECHNOLOGY*, 90(5):629–635, 2009.
- [4] Lindsey C. Teaters and Francine Battaglia. On the computational modeling of unfluidized and fluidized bed dynamics. *J. Fluids Eng.*, 136(10), 2014.
- [5] S.M. Högberg and T.S. Lundström. Motion of dispersed carbon nanotubes during impregnation of fabrics. *Plastics, Rubber and Composites: Macromolecular Engineering*, 40(2):70–79, 2011.
- [6] T.S. Lundström and V. Frishfelds. Modeling filtration of particulate flow during impregnation of dual-scale fabrics. *Journal of Composite Materials*, 47(15):1907–1915, 2013.
- [7] Allan Carlsson, Fredrik Lundell, and L. Daniel Söderberg. Fiber orientation control related to papermaking. *J. Fluids Eng.*, 129(4):457–465, 2006.

- [8] Ali Vakil and Sheldon I. Green. Numerical study of two-dimensional circular cylinders in tandem at moderate reynolds numbers. *J. Fluids Eng.*, 135(7):071204–071204–9, 2013.
- [9] Y. Feng and C. Kleinstreuer. Analysis of non-spherical particle transport in complex internal shear flows. *Physics of fluids*, 25, 2013.
- [10] Clement Kleinstreuer and Yu Feng. Computational analysis of non-spherical particle transport and deposition in shear flow with application to lung aerosol dynamics - a reveiw. *Journal of Biochemical Engineering*, 135:021008–19, 2013.
- [11] Alireza Dastan, Omid Abouali, and Goodarz Ahmadi. Cfd simulation of total and regional fiber deposition in human nasal cavities. *Journal of Aerosol Science*, 69:132–149, 2014.
- [12] C. A. Poland, R. Duffin, I. Kinloch, A. Maynard, W. A. H. Wallace, A. Seaton, V. Stone, S. Brown, W. MacNee, and K. Donaldson. Carbon nanotubes introduced into the abdominal cavity of mice show asbestos-like pathogenicity in a pilot study. *Nat. Nanotechnol.*, 3(7):423–438, 2008.
- [13] O. Cauchois, F. Segura-Sanchez, and G. Ponchel. Molecular weight controls the elongation of oblate-shaped degradable poly(γ -benzyl-l-glutamate)nanoparticles. *Int J Pharm.*, 452(1-2):292–299, 2013.
- [14] Julie A. Champion, Yogesh K. Katare, and Samir Mitragotri. Particle shape: A new design parameter for micro- and nanoscale drug delivery carriers. *Conference: 4th International Nanomedicine and Drug Delivery Symposium Location: Omaha, NE Date: OCT 08-10, 2006 JOURNAL OF CONTROLLED RELEASE*, 121(1-2):3–9, 2007.
- [15] David I. Verrelli. Convenient formulæ for the drag on a prolate ellipsoid moving along its axis of symmetry perpendicular to a plane surface. *International Journal of Multiphase Flow*, 65:138–142, 2014.
- [16] E. R. Weibel. Morphometry of the human lung. *Academic Press, New York.*, 1963.
- [17] S. M. Högberg, H. O. Åkerstedt, T. S. Lundström, and J. F. Freund. Respiratory deposition of fibers in the non-inertial regime: development and application of a semi-analytical model. *Aerosol Sci. Technol*, 44(10):847–860, 2010.

- [18] H. Risken. The fokker-planck equation. *Springer-Verlag, Berlin.*, 1977.
- [19] H. O. Åkerstedt, S. M. Högberg, T. S. Lundström, and T. Sandström. The effect of cartilaginous rings on particle deposition by convection and brownian diffusion. *Natural Sci.*, 2(7):769–779, 2010.
- [20] H. O. Åkerstedt, S. M. Högberg, and T. S. Lundstrom. An asymptotic approach of brownian deposition of nanofibres in pipe flow. *Theor. Comput. Fluid Dyn.*, 27:561–575, 2013.
- [21] B. Asgharian, C. P. Yu, and L. Gradon. Diffusion of fibers in tubular flow. *Aerosol Sci. Technol*, 9(3):213–219, 1988.
- [22] B. E. Dahneke. Slip correction factors for nonspherical bodies - i. introduction and continuum flow. *J. Aerosol Sci.*, 4:139–145, 1973.
- [23] G. B. Jeffery. The motion of ellipsoidal particles immersed in a viscous fluid. *Proc. R. Soc. London.*, 102(175):161–179, 1922.
- [24] B. E. Dahneke. Slip correction factors for nonspherical flow - ii. free molecule flow. *J. Aerosol Sci.*, 4:147–161, 1973.
- [25] E. R. Weibel. *Morphology of the human lung*. Academic Press, New York, 1963.
- [26] D. Keith Walters, Greg W. Burgreen, Robert L. Hester, David S. Thompson, Davis M. Lavalley, Willian A. Pruett, and Xiao Wang. Cyclic breathing simulations in large-scale models of the lung airway from the oronasal opening to the terminal bronchioles. *J. Fluids Eng.*, 136:101101–10, 2014.

Modelling transport and deposition
of non-spherical micro- and
nano-particles in composites
manufacturing

Authors:

Elise Holmstedt, Hans O. Åkerstedt, T. Staffan Lundström

Manuscript

Modelling transport and deposition of non-spherical micro- and nano-particles in composites manufacturing

Elise Holmstedt, Hans O. Åkerstedt, T. Staffan Lundström

Division of Fluid and Experimental Mechanics, Luleå University of Technology,
SE-971 87 Luleå, Sweden

Abstract

In some methods to produce fibre reinforced polymer composites a fabric is impregnated with a fluid that may contain particles on the micro- and nano scales aimed at giving the final product additional properties. It is therefore interesting to be able to reveal how the distribution and orientation of such particles are affected by the processing condition. During the manufacturing of the fabric and during the subsequent lay-up in a mould relatively large channels are formed between bundles of fibres where the impregnating fluid flows; there are also micro channels within the bundle that are also impregnated by the fluid and the capillary action from the larger channels to the micro-channels may be modelled as a suctioning force. Therefore in this study the channel between the bundles are represented as a tube with a circular diameter and a flow field with a perpendicular suctioning component. The effects of all the major forces, the Brownian, gravitational and hydrodynamic forces, acting on the particles are studied and their effects are evaluated, both on single particles and as a statistical aggregate on particle deposition in the channel wall.

1 Introduction

Interest is growing in the development of smart multi-scale composites in which nano-particles are used together with the traditional micro-scale reinforcing fibres to increase the functionality of the composite. This includes enhanced mechanical and electrical properties [1], self-healing ability [2] and energy storage capability [3]. In this context the understanding of the mechanisms governing nano-particle distribution and orientation is crucial not only to optimize the functionality [4] but also in order to avoid problems during the manufacturing such as clogging and uneven flow. Experiments have shown that the initial degree of dispersion of carbon nano-fibres matters [5], and it is obvious that the flow during impregnation is of importance as well. Most fabrics used in structural composites have dual-scale porosity, $< 10\text{ }\mu\text{m}$ for pores within fibre bundles and $> 100\text{ }\mu\text{m}$ for the space between the bundles. In many cases pores on both scales are in the form of long relatively straight channels. The dual-scale porosity may lead to filtration of spherical micro-particles when the carrying fluid moves from one scale to another at the wetting flow front and in the saturated flow [6, 7, 8]. Little is known, however, of the motion of non-spherical micro and nano-sized particles during composites manufacturing. Nano-particles may, for instance, experience both Brownian translational and rotational motion. Fan and Advani [9] experimentally characterized the orientation of carbon nano-tubes (CNTs) subjected to shear flow using TEM. Högberg et al. [10] modelled the motion of single CNTs in saturated flow within the fibre bundles (micro-scale) and between the bundles (meso-scale). Results suggest that nano-fibre displacement and orientation is mainly deterministic on the meso-scale, while typically random on micro-scale; the randomizing Brownian torque may still influence the motion and trigger the fibre to flip in the former, though, when acting together with the fluid shear. Another result was that fibre deposition may lead to a total blockage of the flow within the micro-channels, whereas only minor deposition is expected in the meso-channels. The filtration of spherical micro-particles in saturated flow through dual-scale porous media has been studied by several researchers [11, 12, 13, 14].

In the present work we consider nano-particle motion also at the wetting front with usage of a model geometry mimicking capillary driven flow from the inter-bundle channels to the micro-channels.

2 Simulation set-up

A steady laminar fully developed parabolic flow field with a radial suctioning component is assumed to move in the positive y -direction in a cylindrical pipe with the inlet in the $y = 0$ plane. A non-dimensional representation of the geometry can be seen in Figure 1.

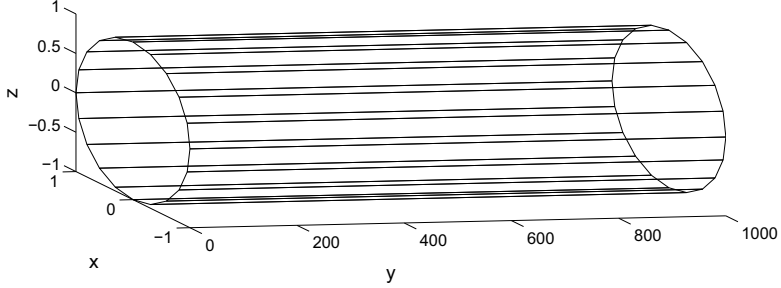


Figure 1: A representative sketch of the geometry used in the simulations.

2.1 Flow field

In fibre reinforced composites made by liquid moulding processes like RTM and vacuum infusion the fibres are often gathered in bundles and during impregnation three main states of the flow may appear. The flow is leading within the bundles, the flow is moving at equal rate within the bundles and between them and the flow is leading in the channels between the bundles. In the first case capillary action dominates over any applied pressure gradient. In the second case the applied pressure gradient is matched to the capillary pressure and in the third case, being the focus in this study an applied pressure gradient dominates over the capillary action. If we now concentrate on fibre bundles being directed with the main flow the channels between the bundles are first filled and then capillary action will be the main reason for the filling of the bundles[8]. To model this capillary transport of fluid into the bundles a specified suction from the channel into the bundles is considered.

In the limit of small Re number $Re = U_0 a / \nu \ll 1$ and axis-symmetry the Navier-Stokes equation can be reduced to one equation for the stream function Ψ of the form

$$\left(r \frac{\partial}{\partial r} \left(\frac{1}{r} \frac{\partial}{\partial r} \right) + \frac{\partial^2}{\partial y^2} \right)^2 \Psi = 0. \quad (1)$$

The velocity component can then be expressed as

$$u = \frac{1}{r} \frac{\partial \Psi}{\partial r} \quad (2)$$

$$V = -\frac{1}{r} \frac{\partial \Psi}{\partial y} \quad (3)$$

Equations 1 - 3 are made dimensionless by $y = \bar{y}/a$ and $r = \bar{r}/a$ where a is the radius of the channel.

The suction at the wall V_0 is considered small and a small parameter $\varepsilon = V_0/U_0 < 1$ is introduced. The variation in the streamwise direction can then be considered small and therefore a slow variable $Y = \varepsilon y$ is introduced. Equation (1) can then be solved using a perturbation analysis leading to the flow field

$$u_0(\bar{r}, \bar{y}) = \left(U_0 - 4V_0\varepsilon \frac{\bar{y}}{a} \right) \left(1 - \left(\frac{\bar{r}}{a} \right)^2 \right) \quad (4)$$

$$V(\bar{r}, \bar{y}) = -\varepsilon V_0 \left(\left(\frac{\bar{r}}{a} \right)^4 - 2 \left(\frac{\bar{r}}{a} \right)^2 \right). \quad (5)$$

In these equations $u_0(\bar{r}, \bar{y})$ is the velocity component in the direction of the channel and $V(\bar{r}, \bar{y})$ the corresponding radial velocity component.

2.2 Particle equations of motion

The model for the motion of the particles used in this work was originally presented in [14]. Two coordinate systems are defined to describe the movement of the particles, global coordinates $[x, y, z]$, and local ones $[x', y', z']$ fixed to the particle with the polar axis along z' . The rotation matrix \mathbf{A} transforms from local to global coordinates via $x' = \mathbf{A}x$. Note that all primed quantities refer to the particle coordinate frame.

When small Stokes numbers (St) apply for the particles, inertia may be neglected and the particle equations of motion are reduced to

$$F_i^h + F_i^g + f_i^{Br} = 0 \quad (6)$$

$$T_{i'}^h + T_{i'}^{Br} = 0 \quad (7)$$

in which F_i^h , F_i^g and F_i^{Br} are the hydrodynamic, gravitational and Brownian forces and $T_{i'}^h$ and $T_{i'}^{Br}$ are the hydrodynamic and Brownian torques.

The hydrodynamic force acting on the particles considered in this study may be expressed as

$$\mathbf{F}^h = 3\pi\mu\mathbf{A}^T \begin{bmatrix} d_{\perp} & 0 & 0 \\ 0 & d_{\perp} & 0 \\ 0 & 0 & d_{\parallel} \end{bmatrix} \mathbf{A} \begin{bmatrix} u - \frac{dx}{dt} \\ v - \frac{dy}{dt} \\ w - \frac{dz}{dt} \end{bmatrix} \quad (8)$$

In this equation μ is the dynamic viscosity of the fluid, $[u, v, w]$ are the components of the fluid velocity, $[\frac{dx}{dt}, \frac{dy}{dt}, \frac{dz}{dt}]$ the components of the particle velocities and \mathbf{A} is the rotation matrix between the local and global coordinates [14].

When the effect of the gravitational force is taken into account in the simulations it is defined as

$$F_z^g = \pi\rho_f g d_f^3 \beta / 6, \quad (9)$$

where ρ_f is the density of the particle and g is the gravitational acceleration. Particle density is usually much greater than the surrounding fluid and thus buoyancy can be neglected. The gravitational force is defined in the positive z -direction.

The Brownian force is modelled as an independent zero-mean Gaussian white-noise process, which for spheroids takes the following form

$$F_{i'}^{Br}(t) = \chi_{i'}^t \sqrt{\frac{2D_{i'}^t}{\delta t}}, \quad (10)$$

where

$$D_{i'}^t = \frac{\sigma T}{3\pi\mu d_{i'}} \quad (11)$$

is the Brownian translational diffusion coefficient, $\chi_{i'}^t$ is normally distributed random numbers, δt is a Brownian time increment, σ is the Boltzmann constant and T is the absolute temperature.

2.2.1 Stokes diameters

Both the Hydrodynamic and Brownian force are dependent on the Stokes diameters d_{\perp} and d_{\parallel} , oriented perpendicular and parallel respectively. The

stokes diameters for a prolate spheroid are given by

$$\frac{d_{\perp}}{d_f} = \frac{\frac{8}{3}(\beta^2 - 1)}{C_{\perp}^t \left[\frac{2\beta^2 - 3}{\sqrt{\beta^2 - 1}} \ln(\beta + \sqrt{\beta^2 - 1}) + \beta \right]} \quad (12)$$

$$\frac{d_{\parallel}}{d_f} = \frac{\frac{4}{3}(\beta^2 - 1)}{C_{\parallel}^t \left[\frac{2\beta^2 - 3}{\sqrt{\beta^2 - 1}} \ln(\beta + \sqrt{\beta^2 - 1}) - \beta \right]}, \quad (13)$$

and the ones for oblate spheroids are given by [15]

$$\frac{d_{\perp}}{d_f} = \frac{\frac{8}{3}(\beta^2 - 1)}{C_{\perp}^t \left[\frac{\beta(3\beta^2 - 2)}{\sqrt{\beta^2 - 1}} \arctan(\sqrt{\beta^2 - 1}) \right]} \quad (14)$$

$$\frac{d_{\parallel}}{d_f} = \frac{\frac{4}{3}(\beta^2 - 1)}{C_{\parallel}^t \left[\frac{\beta(3\beta^2 - 2)}{\sqrt{\beta^2 - 1}} \arctan(\sqrt{\beta^2 - 1}) \right]}. \quad (15)$$

Here d_f is the geometric diameter and β is the aspect ratio. Note that $\beta > 1$ for both oblate and prolate spheroids so the replacement of $\beta \rightarrow 1/\beta$ is made when going from prolate to oblate spheroid.

No exact expression for the slip correction factors C_{\parallel}^t and C_{\perp}^t for the fluid dynamic drag when the diameters of the particles approaches that of the mean free drag of air molecules exists but an approximate method by Dahneke [16] is applied.

2.3 Numerical set-up for simulation of impregnation of composites

The channel between fibre bundles are represented in the model by circular pipes with a radius of 0.1 mm and a length of 0.1 m aligned along the y -axis and with the inlet in the $y = 0$ plane.

The inlet velocity U_{00} of the fluid was set to 10 $\mu\text{m/s}$ as per experiments done by Nordlund et. al. [8]. Three different suction factors were used during the experiments. In the first case $\varepsilon = 0$ corresponding to no suction, in the second case $\varepsilon = 0.0002$ which corresponds to all the fluid passing through the channel wall and the outlet velocity being zero after 1.25 m and $\varepsilon = 0.001$ corresponding to the same happening after 0.25 m.

The resin was set to have a density of 1000 kg/m^3 and the particles a density of 1950 kg/m^3 .

Deposition results are based on simulations with 10000 particles whose starting positions are randomly distributed evenly across the inlet of the

channel and are run until all particles have either been deposited by reaching the wall of the channel or exited the outlet.

The simulation time step δt was set to 20 ms after a careful study of the Brownian dispersion.

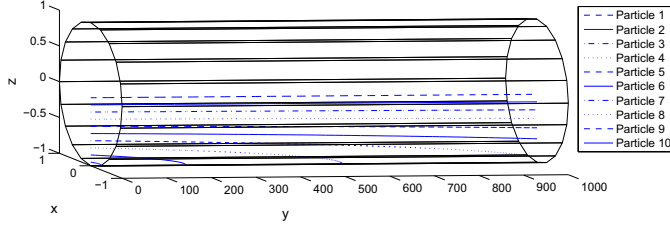
3 Results

To understand the deposition of particles of different geometries in composite manufacturing it is necessary to study which effect different forces have on the particles.

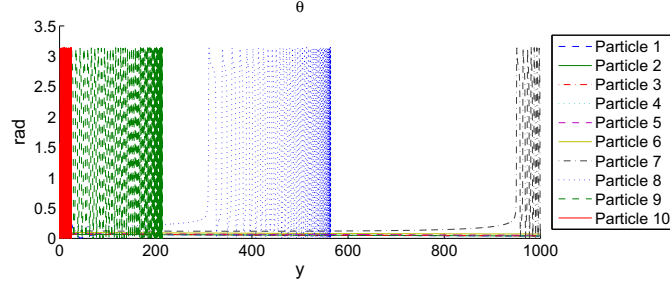
3.1 Single particle tracking

To start with ten prolate particles with $\beta = 3$ were placed, evenly spaced, on the negative z -axis in the inlet of the channel. The particle tracks of most of the particles are straight indicating that these particles are unaffected by the suction at the walls $\varepsilon = 0.001$, see Figure 2a. It is at the same time obvious that the tracks of particles 7-10, that are closest to the wall, are strongly dependent on the suction and they intercept with the wall within the region studied. To study the rotations the particles experience it is convenient to investigate the θ -angle being the angle between the particles polar z' -axis and the y -axis of the flow. As the starting position is perpendicular to the flow, all particles start at $\theta = \pi/2$ but soon rotate towards $\theta = 0$. All particle rotation can be seen in Figure 2b where it is discernible that the particles start to rotate in so called Jeffery orbits [17] whose frequency intensifies before they are intercepted by the wall. A clearer picture of the process can be seen by studying the first 3 mm in Figure 2c. Here it is obvious that all particles initially rotate to orientate with the flow, where particle 10 starts to rotate with very frequent Jeffery orbits. At the same time particle 9 can also be seen to start to rotate, although with a slower frequency. By studying Figure 2c carefully it is also clear that the resting angle of the particles are not at $\theta = 0$ but slightly higher as the flow field is not completely parallel to the channel.

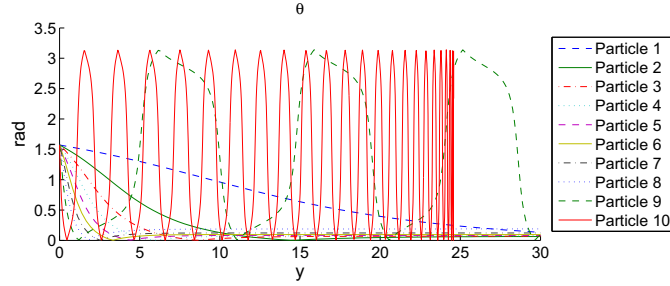
When oblate particles with the same size and β as the prolate particles in Figure 2 are released the traces the mass centres leave are practically the same as the prolate particles but an interesting phenomena occurs in the rotation of the particles. In Figure 3a the angle θ , the angle between the polar axis of the oblate particles and the flow, can be seen, and in Figure 3b a zoom in on the first 6 mm. Oblate particles close to the channel wall start to experience Jeffery orbits, but stop suddenly before intercepting the wall.



(a) Trace of prolate particles equally spaced along the negative z -axis in the inlet of the channel.

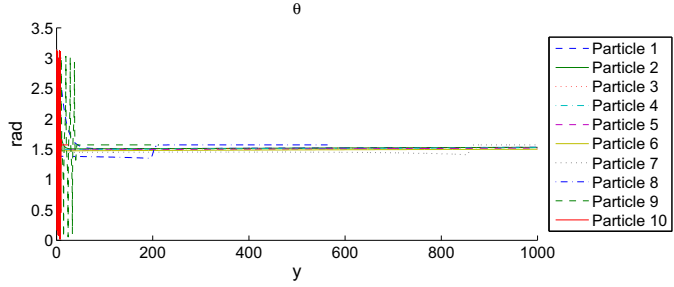


(b) The θ -angle between the particles in 2a and the channels y -axis.

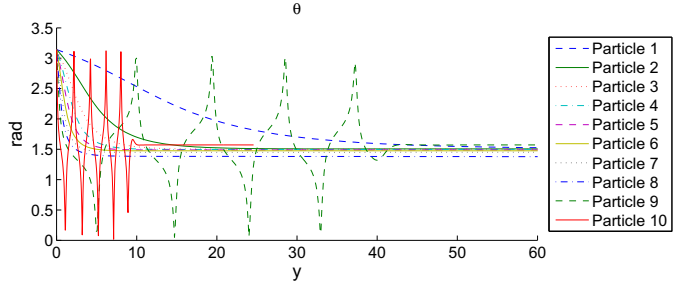


(c) The first 3 mm of the θ -angle between the particles in 2a and the channels y -axis.

Figure 2: Simulations of 10 prolate particles only influenced by a suctioning flow field.

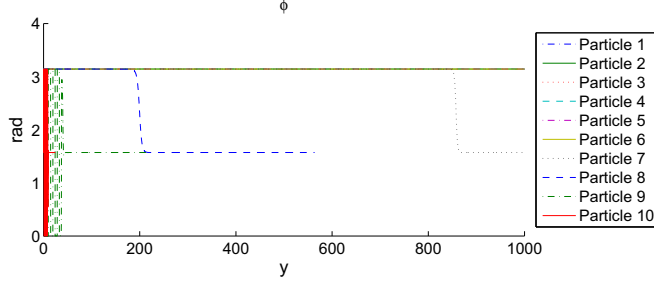


(a) The θ -angle between oblate particles and the channels y -axis.

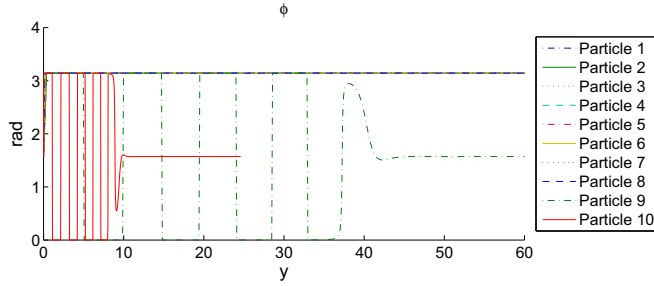


(b) The first 6 mm of the θ -angle between the oblate particles and the channels y -axis.

Figure 3: Simulations of 10 oblate particles only influenced by a suctioning flow field.



(a) The ϕ -angle between oblate particles and the channels y -axis.



(b) The first 6 mm of the ϕ -angle between the oblate particles and the channels y -axis.

Figure 4: Simulations of 10 oblate particles only influenced by a suctioning flow field.

To understand this phenomena it is necessary to scrutinize the other angle describing the particles rotation, the ϕ -angle. This angle describes the tilt of the particles polar axis against the flow; i.e. if the particle is facing up, down or to the side. While the particles are rotating in Jeffery orbits with change of θ the angle ϕ displays a binary behaviour, the particle is facing 'up' to then switch instantaneously 'down', as seen in Figure 4. At a certain point the particle rotates with $\phi = \pi/2$ so that the polar axis of the particle is now perpendicular to both the vertical and radial component of the flow. There is now no difference in pressure between the two sides of the particle and thus no Jeffery orbits. This occurs at the point where the radial component of the flow field is large enough so that the oblate particle will want to orient itself after it. The radius of this point is smaller further into the channel as the vertical velocity component is smaller which is the reason particles 1 to 8 experience no Jeffery orbits.

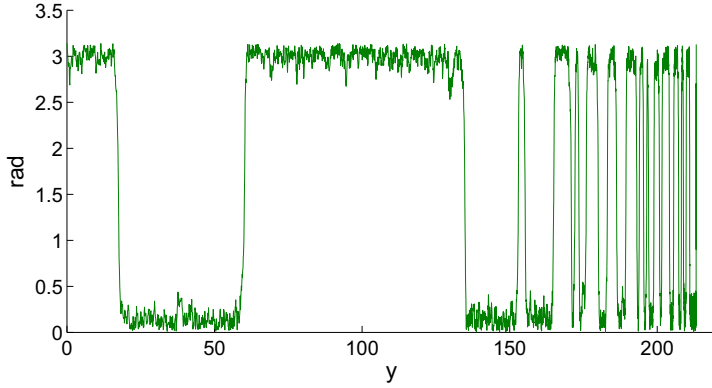


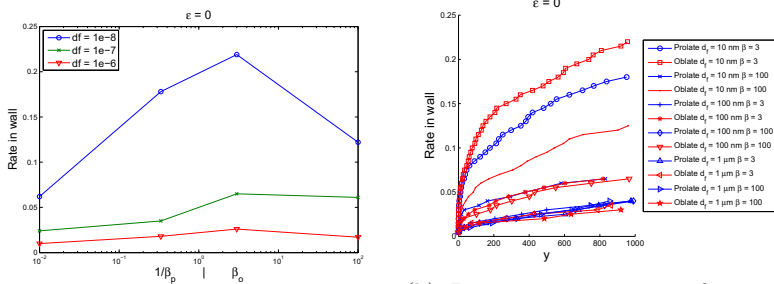
Figure 5: θ angle of a prolate particle influenced by Brownian motion released near the wall of the channel.

When introducing Brownian motion into the calculations to see the effect it has on particles rotation as they travel through the flow field a large prolate particle with $d_f = 1 \mu\text{m}$ and $\beta = 100$ is studied. It is released in the same position as particle 9 in 2a and the angle θ is recorded in Figure 5. As can be seen it exhibits a similar pattern to that of a prolate particle with much smaller β not affected by Brownian motion, although the pattern is not as regular.

With so large particles the lateral Brownian forces are so small that the difference in the trace left by the mass center of the particle is visually indistinguishable from a particle not affected by Brownian motion.

3.2 Statistical deposition rates

Statistical deposition rates are first studied for a channel with no suction for different particle geometries. As one can see in Figure 6a the deposition for this type of channel varies between 2% and 20% with the highest deposition occurring for smaller particles and particles with a smaller aspect ratio β . Note that prolate particles are plotted against the inverse of β as to make it easier to compare them visually with the oblate particles. In Figure 6b the deposition rates can be seen plotted as a function of channel length. Since only Brownian forces act on the particles perpendicular to the flow it is expected that there is a higher deposition rate for smaller particles. It is also clear that particles with a larger aspect ratio have a dampening effect on Brownian dispersion, as do prolate particles as compared to oblate ones.



(a) Deposition rates as a function of β . (b) Deposition rates as a function of channel length.

Figure 6: Deposition rates in a channel with no suction for particles with different size and shape.

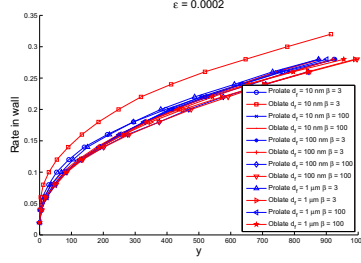
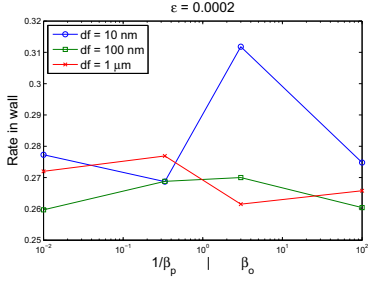
When suction is introduced in the channel it takes over as the dominating mechanism acting on the particles in the plane perpendicular to the channel and the deposition rates increase overall. For channels with a suction factor of $\varepsilon = 0.0002$ the deposition rates are fairly constant for all particles at about 27% as can be seen in Figure 7 but one can still discern a slight increase in deposition for the smallest oblate particles with $\beta = 3$.

The deposition rates for particles in a channel with a suction factor of $\varepsilon = 0.001$ vary very little between particle types and is about 57% as can be seen in Figure 8.

3.3 Gravitational effects

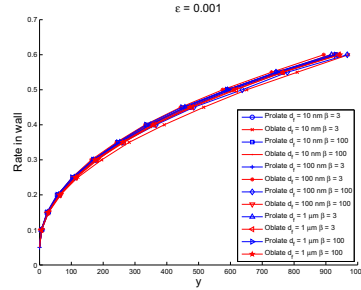
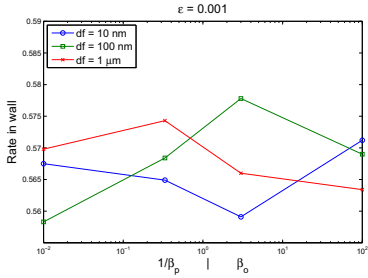
It is clear that gravity greatly influences the deposition rates of particles suspended in a horizontal flow. When doing deposition studies with gravitational effects perpendicular to the flow included in the simulations it is clear that gravity has a great influence on particle deposition. A combination of a relatively high particle density and a slow fluid flow gives the particles ample time to reach the border of the channel. Only particles with a geometric diameter of 10 nm and 100 nm were used in this study since a heavier particle was deposited almost instantaneously but even for the smaller particles the deposition rate was 100% over the length of the channel.

It is, however, interesting to study the deposition patterns of a variety of particles. In Figure 9 the traces of 20 randomly distributed oblate and prolate particles with a geometric diameter of 10 nm and $\beta = 100$ can be seen. It is clear that the geometry of the particles affect how far they follow the flow of the channel.



(a) Deposition rates as a function of β . (b) Deposition rates as a function of channel length.

Figure 7: Deposition rates in a channel with a suction factor of $\varepsilon = 0.0002$ for particles with different size and shape.



(a) Deposition rates as a function of β . (b) Deposition rates as a function of channel length.

Figure 8: Deposition rates in a channel with a suction factor of $\varepsilon = 0.001$ for particles with different size and shape.

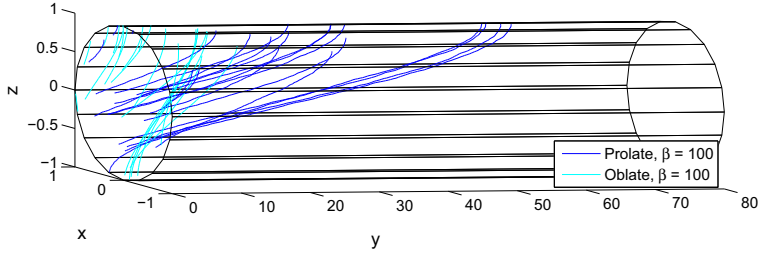


Figure 9: Traces of oblate and prolate nano-particles affected by gravity.

In Figure 10 the deposition rate as a function of the y -axis for a variety of particles influenced by gravity are plotted for a channel flow with a suction factor of $\varepsilon = 0.001$. It is clear that prolate particles travel much further into the channel than the respective oblate particles. It is also clear that for both oblate and prolate particles the ones with a small β reach the furthest with the spherical particles reaching the furthest of all. This pattern is seen for both particles with a geometric diameter of 100 nm and 10 nm although the latter is being transported for an order of magnitude longer.

Comparing the gravitational deposition rates in a channel with suction in Figure 10 and in a channel without in Figure 11 there is no noticeable change in deposition patterns.

4 Conclusions

A semi-analytical model describing the motion of oblate and prolate spheroids on the nano and micro scales has been developed, and simulations enabling both single particle tracking and aggregation of multiple particle deposition were carried out. In this work this model was applied on composite manufacturing and simulating the impregnation process taking into account capillary forces creating a suctioning effect through the wall of the channels in the fabric. However, the model can be applied on a variety of cases where Reynolds and Stokes particle numbers are small.

It is clear that while particle shape has a great influence on deposition rates in a flow moving strictly in the direction of the channel, as soon as a perpendicular suctioning force is added these changes seem to disappear. This is due to the dispersion affecting particles from the Brownian force being relatively small compared to the dispersion from the suctioning force; if a certain percentage of the fluid is going into the walls of the channel that percentage of particles are going to follow it.

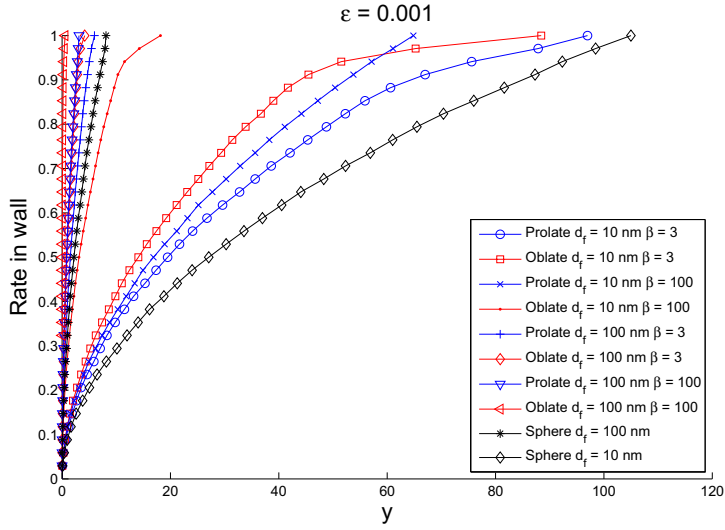


Figure 10: Depositions of nano-particles of varying size and shape.

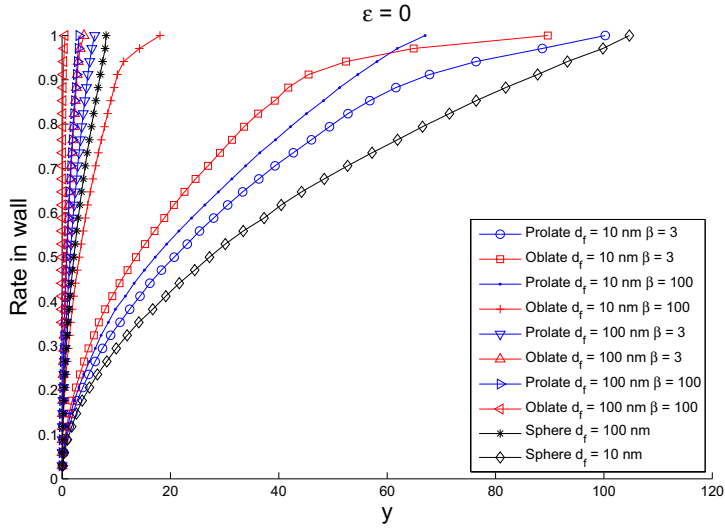


Figure 11: Depositions of nano-particles of varying size and shape in a channel with no suction.

During the gravitational studies an effect of particle geometry is clear. Although this combination of slow flow field and high particle density ensure that the deposition rates are always 100 % the deposition patterns vary greatly with geometry. It is interesting to compare this study to the one without gravity and without suction and note that while the Brownian dispersion ensures the highest deposition rates for particles with low β , for the gravitational settling this is reversed. In a fluid with lower density, thus increasing the Brownian dispersion, and with a lower particle density, decreasing the gravitational effects, these effects may cancel each other out.

Looking at a single particle only influenced by a flow field it is clear that particle geometry, although it does not influence the path of the mass centre, has a great influence on the rotation of the particle. Prolate particles orient themselves with the polar axis parallel to the flow where they display Jeffery orbits whose frequency increases with smaller β and increased proximity to the channel wall. Oblate particles also orient themselves with the flow, although their geometry necessitates that their polar axis is perpendicular with the flow and pointing at the center of the channel. Unlike the prolate particles the oblate particles position is affected close the wall of the channel where the particles tilt so the polar axis is perpendicular both to the vertical and radial component of the flow-field.

5 Acknowledgement

The authors would like to thank the Swedish Research Council for funding this work.

References

- [1] Malte H. G. Wichmann, Jan Sumfleth, and Florian H. Gojny. Glass-fibre-reinforced composites with enhanced mechanical and electrical properties - benefits and limitations of a nanoparticle modified matrix. *Conference: 4th Conference on Fracture of Polymers, Composites and Adhesives Location: Les Diablerets, Switzerland*, 2005.
- [2] M. R. Kessler, N. R. Sottos, and S. R. White. Self-healing structural composite materials. *Composites part a-applied science and manufacturing*, 34(8):743–753, 2003.
- [3] L. E. Asp and E. S. Greenhalgh. Structural power composites. *Composites science and technology*, 101:41–61, 2014.

- [4] E. T. Thostenson, J.J.J. Gangloff, C. Li, and J-H. Byun. Electrical anisotropy in multiscale nanotube/fiber hybrid composites. *Applied Physics Letters*, 95(7):073111–3, 2009.
- [5] Z. Fan, K-T. Hsiao, and S. G. Advani. Experimental investigation of dispersion during flow of multi-walled carbon nanotube/polymer suspension in fibrous porous media. *Carbon*, 25(1):871–6, 2004.
- [6] S. P. Fernberg, E. J. Sandlund, and T. S. Lundstrom. Mechanisms controlling particle distribution in infusion molded composites. *Journal of Reinforced Plastics and Composites.*, 42(4):871–6, 2006.
- [7] M. Nordlund, E. J. Sandlund, and T. S. Lundstrom. Particle deposition mechanisms during processing of advanced composite materials. *Composites: Part A*, 38(10):2182–93, 2007.
- [8] M. Nordlund and T. S. Lundstrom. An investigation of particle deposition mechanisms during impregnation of dual-scale fabrics with micro particle image velocimetry. *Polymer Composites*, 31:5232–40, 2010.
- [9] Z. Fan and S. G. Advani. Characterization of orientation state of carbon nanotubes in shear flow. *Polymer*, 46(14):5232–40, 2005.
- [10] S.M. Högberg and T.S. Lundström. Motion of dispersed carbon nanotubes during impregnation of fabrics. *Plastics, Rubber and Composites: Macromolecular Engineering*, 40(2):70–79, 2011.
- [11] W. R. Hwang, S. G. Advani, and S. Walsh. Direct simulations of particle deposition and filtration in dual-scale porous media. *Composites part a-applied science and manufacturing*, 42(10):1344–1352, 2011.
- [12] V. Frishfelds and T. S. Lundstrom. Modelling of particle deposition during impregnation of dual-scale fabrics. *Plastics, Rubber and Composites: Macromolecular Engineering.*, 2011.
- [13] T.S. Lundström and V. Frishfelds. Modeling filtration of particulate flow during impregnation of dual-scale fabrics. *Journal of Composite Materials*, 47(15):1907–1915, 2013.
- [14] S. M. Högberg, H. O. Åkerstedt, T. S. Lundström, and J. F. Freund. Respiratory deposition of fibers in the non-inertial regime: development and application of a semi-analytical model. *Aerosol Sci. Technol*, 44(10):847–860, 2010.

- [15] Elise Holmstedt, H. O. Åkerstedt, and T. S. Lundstrom. Modelling transport and deposition rate of oblate and prolate nano- and micro particles in a virtual model of the human airway. *Submitted*, 2014.
- [16] B. E. Dahneke. Slip correction factors for nonspherical bodies - i. introduction and continuum flow. *J. Aerosol Sci.*, 4:139–145, 1973.
- [17] G. B. Jeffery. The motion of ellipsoidal particles immersed in a viscous fluid. *Proc. R. Soc. London.*, 102(175):161–179, 1922.

